Journal of Computational Physics 230 (2011) 6688–6708

Contents lists available at ScienceDirect

Journal of Computational Physics

journal homepage: www.elsevier.com/locate/jcp

Topology optimization of unsteady incompressible Navier–Stokes flows

Yongbo Deng [a,b], Zhenyu Liu [a,*], Ping Zhang [a], Yongshun Liu [a,b], Yihui Wu [a]

[a] State Key Laboratory of Applied Optics, Changchun Institute of Optics, Fine Mechanics and Physics (CIOMP), Chinese Academy of Sciences, 130033 Changchun, Jilin, China
[b] Graduate University of Chinese Academy of Sciences, Beijing, China

ARTICLE INFO

Article history:
Received 15 November 2010
Received in revised form 29 April 2011
Accepted 4 May 2011
Available online 10 May 2011

Keywords:
Topology optimization
Unsteady flow
Navier–Stokes equations
Continuous adjoint method

ABSTRACT

This paper discusses the topology optimization of unsteady incompressible Navier–Stokes flows. An optimization problem is formulated by adding the artificial Darcy frictional force into the incompressible Navier–Stokes equations. The optimization procedure is implemented using the continuous adjoint method and the finite element method. The effects of dynamic inflow, Reynolds number and target flux on specified boundaries for the optimal topology of unsteady Navier–Stokes flows are presented. Numerical examples demonstrate the feasibility and necessity of this topology optimization method for unsteady Navier–Stokes flows.

1. Introduction

Layout optimization of fluidic devices is an interesting field with respect to theory and application. The goal of optimization is to achieve better performance for a user specified objective that is related to certain characteristics of fluidic problems. Usually, layout optimization is categorized into shape optimization and topology optimization. Shape optimization improves the performance of a fluidic device by adjusting the positions of structural boundaries, keeping the topology of the structure unchanged. Topology optimization can optimize the shape and the topology of structures simultaneously. Therefore, topology optimization is a more general optimization technique than shape optimization. Currently, the density type method [1,2] and level set method [3–6] have been developed for implementing of topology optimization. Topology optimization by the density method was first used to design stiffness and compliance mechanisms [7–10] and has been extended to multiple physical problems, such as acoustic, electromagnetic, fluidic, optical and thermal problems [11–17]. Topology optimization by the density method for fluidic problems was first researched for Stokes flows [12,18,19] and Darcy–Stokes flows [20,21]. It was later extended to Navier–Stokes flows [22–26] and non-Newtonian flows [27]. Additionally, the topology optimization method has been applied to design fluidic devices [28–31]. The level set method, pioneered by Osher and Sethian [32], accomplishes the change of topology by evolving and merging the zero contour of the level set function. This method provides a general way to track the implicit interface between two phases, and it has been applied to fluidic shape and topology optimization [25,26]. One of the major advantages of the level set method lies in expressing continuously moving interfaces and abstracting the material domains that correspond to the structural topology. Recently, it has been observed that the conventional level set method may be inadequate for the cases in which the initial shape of the structure has fewer holes than the optimal geometry [4], especially in two-dimensional cases. The above difficulty can be

* Corresponding author.
E-mail address: liuzy@ciomp.ac.cn (Z. Liu).

0021-9991/$ - see front matter © 2011 Elsevier Inc. All rights reserved.
doi:10.1016/j.jcp.2011.05.004

overcome using topological sensitivity, which was introduced by Sokolowski and Zochowski [33] for linear elasticity and that has been extended to several other linear and nonlinear physical problems [34–37]. In particular, the topological sensitivity has been researched for steady Stokes flows [38–41] and Navier–Stokes flows [42]. To the best of the authors' knowledge, there is no formally published paper discussing the topological sensitivity for unsteady Navier–Stokes flows. Therefore, the application of the level set method to topology optimization of the unsteady flows is limited.

Until recently, the topology optimization of fluidic flows has focused primarily on steady flows. In contrast, unsteady flows are widespread in reality, and the optimization of unsteady flows using the shape optimization method has been researched [43–45]. As such, it is desirable to extend topology optimization to the area of unsteady Navier–Stokes flows. In this paper, the density type topology optimization method is extended to unsteady incompressible Navier–Stokes flows at low and moderate Reynolds numbers based on work by Borrvall and Petersson [12] and Gersborg-Hansen et al. [22]. The optimization problem with a general objective is analyzed by the continuous adjoint method. Recently, Kreissl et al. implemented the topology optimization of unsteady flows [46]. In Kreissl's work, the optimization problem is analyzed using the stabilized SUPG and PSPG finite element formulation and the corresponding discretized adjoint equations. In this paper, the topology optimization problem with more general objectives is analyzed using the continuous adjoint method. Based on the Navier–Stokes equations and the derived continuous adjoint equations, the optimization can be implemented by choosing any stable spatial discretization method and adaptive temporal discretization method, such as the finite difference method, the finite element method or the finite volume method. In this paper, the numerical discretization of the Navier–stokes equations and the adjoint equations is implemented using the standard finite element method with Taylor-Hood element.

This paper is organized as follows: the variational problem of topology optimization for unsteady incompressible Navier–Stokes flows is stated in Section 2; the continuous adjoint equations and adjoint sensitivity for the optimization objective are derived in Section 3; the numerical implementation of the optimization method using the standard finite element method is discussed in Section 4; and several numerical examples are presented in Section 5.

2. Topology optimization problem of unsteady incompressible Navier–Stokes flows

The dynamic properties of velocity and pressure for incompressible fluidic flows can be expressed using the incompressible Navier–Stokes equations as [47]

$$\begin{aligned} &\rho\tfrac{\partial \mathbf{u}}{\partial t} - \eta\nabla\cdot(\nabla\mathbf{u}+\nabla\mathbf{u}^{\mathrm{T}}) + \rho(\mathbf{u}\cdot\nabla)\mathbf{u} + \nabla p = \mathbf{f}, \quad \text{in } Q \\ &-\nabla\cdot\mathbf{u} = 0, \quad \text{in } Q \end{aligned} \tag{1}$$

where $\mathbf{u}$ is the fluidic velocity; p is the fluidic pressure; ρ is the fluidic density; η is the fluidic viscosity; $\mathbf{f}$ is the body force loaded on the fluid; and t is the time. $Q = (0,T)\times\Omega$, where $(0,T)$ is the computational time interval and Ω is the computational domain. To solve a transient problem, an initial condition is needed

$$\mathbf{u}(0,\mathbf{x}) = \mathbf{u}_0(\mathbf{x}), \quad \text{in } \Omega \tag{2}$$

where $\mathbf{u}_0(\mathbf{x})$ satisfies the incompressible condition $\nabla\cdot\mathbf{u}_0 = 0$. The commonly used boundary conditions for incompressible Navier–Stokes equations include the Dirichlet and Neumann type boundary conditions

$$\mathbf{u} = \mathbf{u}_D(t,\mathbf{x}), \quad \text{on } \Sigma_D \tag{3}$$

$$[-p\mathbf{I} + \eta(\nabla\mathbf{u}+\nabla\mathbf{u}^{\mathrm{T}})]\mathbf{n} = \mathbf{g}(t,\mathbf{x}), \quad \text{on } \Sigma_N \tag{4}$$

where $\mathbf{u}_D$ and $\mathbf{g}$ are the specified velocity and stress distribution on the boundaries Γ_D and Γ_N; $\mathbf{n}$ is the outward unit normal vector on $\partial\Omega$; $\Sigma_D = (0,T)\times\Gamma_D$; and $\Sigma_N = (0,T)\times\Gamma_N$. Specifically, the no-slip boundary is a particular Dirichlet type boundary condition where $\mathbf{u}_D = \mathbf{0}$, and the open-boundary on the outlet can be expressed by the Neumann type boundary condition as $\mathbf{g} = \mathbf{0}$. In topology optimization of the Navier–Stokes flow, the body force can be expressed as [12,22]

$$\mathbf{f} = -\alpha\mathbf{u} \tag{5}$$

where α is the impermeability of a porous medium. Its value depends on the optimization design variable γ [12,22]

$$\alpha(\gamma) = \alpha_{\min} + (\alpha_{\max} - \alpha_{\min})\frac{q(1-\gamma)}{q+\gamma} \tag{6}$$

where $\alpha_{\min}$ and $\alpha_{\max}$ are the minimal and maximal values of α respectively, and q is a real and positive parameter used to adjust the convexity of the interpolation function in Eq. (6). The value of γ can vary between zero and one, where $\gamma = 0$ corresponds to an artificial solid domain and $\gamma = 1$ to a fluidic domain, respectively. Usually, $\alpha_{\min}$ is chosen as 0, and $\alpha_{\max}$ is chosen as a finite but high number to ensure the numerical stability of the optimization and to approximate a solid with negligible permeability [22,23]. When solving transient incompressible Navier–Stokes equations, the design variable γ is time independent because the layout of fluidic domain is kept unchanged.

Based on the above description, the topology optimization problem for a unsteady incompressible Navier–Stokes flow can be formulated as

$$
\begin{aligned}
&\min \quad J(\mathbf{u},p;\gamma)\\
&\text{s.t.} \quad \rho\tfrac{\partial \mathbf{u}}{\partial t}-\eta\nabla\cdot(\nabla\mathbf{u}+\nabla\mathbf{u}^{\mathrm{T}})+\rho(\mathbf{u}\cdot\nabla)\mathbf{u}+\nabla p=-\alpha\mathbf{u}, \quad \text{in } Q\\
&\quad -\nabla\cdot\mathbf{u}=0, \quad \text{in } Q\\
&\quad \mathbf{u}(0,\mathbf{x})=\mathbf{u}_0(\mathbf{x}), \quad \text{in } \Omega\\
&\quad \mathbf{u}(t,\mathbf{x})=\mathbf{u}_D(t,\mathbf{x}), \quad \text{on } \Sigma_D\\
&\quad [-p\mathbf{I}+\eta(\nabla\mathbf{u}+\nabla\mathbf{u}^{\mathrm{T}})]\mathbf{n}=\mathbf{g}(t,\mathbf{x}), \quad \text{on } \Sigma_N\\
&\quad \int_\Omega \gamma d\Omega\leqslant\theta\cdot V_0, \quad 0\leqslant\gamma\leqslant 1
\end{aligned}
\tag{7}
$$

where $V_0=\int_\Omega 1\ \mathrm{d}\Omega$ is the volume of the whole design domain and $\theta\in(0,1)$ is the upper bound for the volume constraint. A general optimization objective, which includes both the domain and boundary integrations about the unknowns of the Navier–Stokes equations, is chosen to be

$$
J(\mathbf{u},p;\gamma)=\int_0^T\int_\Omega \beta_1 A(\mathbf{u},\nabla\mathbf{u},p;\gamma)\mathrm{d}\Omega\mathrm{d}t+\int_0^T\int_{\partial\Omega}\beta_2 B(\mathbf{u},p;\gamma)\mathrm{d}\Gamma\mathrm{d}t \tag{8}
$$

where β_1 and β_2 are space-independent parameters, respectively.

3. Adjoint analysis of optimization problem

According to the adjoint method for the Navier–Stokes equations in [45,48,49], the adjoint analysis of the topology optimization problem for unsteady Navier–Stokes flows is implemented as follows. Without considering the inequality constraint on the volume of fluidic channels at first, the topology optimization problem in Eq. (7) can be rewritten in the following abstract form:

$$
\min J(\mathbf{u},p;\gamma), \quad \text{s.t.} e(\mathbf{u},p;\gamma)=0, \quad \gamma\in\mathcal{K} \tag{9}
$$

where $\mathcal{K}$ is the set of feasible values of the design variable γ, and $e(\cdot)$ is the weak operator of the Navier–Stokes equations. According to the Karush–Kuhn–Tucker conditions for the partial differential equation constrained optimization problem [45,50], the optimization problem in Eq. (9) can be solved by solving the following equations:

$$
e(\mathbf{u},p;\gamma)=0 \tag{10}
$$

$$
\begin{pmatrix}(e_{\mathbf{u}}(\mathbf{u},p;\gamma))^* & \mathbf{0}\\ \mathbf{0} & (e_p(\mathbf{u},p;\gamma))^*\end{pmatrix}\begin{pmatrix}\boldsymbol{\mu}\\ v\end{pmatrix}=\begin{pmatrix}-J_{\mathbf{u}}(\mathbf{u},p;\gamma)\\ -J_p(\mathbf{u},p;\gamma)\end{pmatrix} \tag{11}
$$

$$
(e_\gamma(\mathbf{u},p;\gamma))^*(\boldsymbol{\mu},v)+J_\gamma(y;\gamma)=0 \tag{12}
$$

where $\boldsymbol{\mu}$ and v are the adjoint variables for the fluid velocity $\mathbf{u}$ and pressure p, respectively, and $(\cdot)^*$ is the adjoint of the corresponding operator. Therefore, according to Eq. (11), the adjoint equations of the Navier–Stokes equations can be written as follows (see Appendix A for more details):

$$
\begin{aligned}
&-\rho\tfrac{\partial\boldsymbol{\mu}}{\partial t}-\eta\nabla\cdot(\nabla\boldsymbol{\mu}+\nabla\boldsymbol{\mu}^{\mathrm{T}})-\rho(\mathbf{u}\cdot\nabla)\boldsymbol{\mu}+\rho(\nabla\mathbf{u})\cdot\boldsymbol{\mu}+\nabla v=-\beta_1\left(\tfrac{\partial A}{\partial\mathbf{u}}-\nabla\cdot\tfrac{\partial A}{\partial\nabla\mathbf{u}}\right)+\tfrac{\partial\mathbf{f}}{\partial\mathbf{u}}\boldsymbol{\mu}, \quad \text{in } Q\\
&-\nabla\cdot\boldsymbol{\mu}=-\beta_1\tfrac{\partial A}{\partial p}+\tfrac{\partial\mathbf{f}}{\partial p}\cdot\boldsymbol{\mu}, \quad \text{in } Q\\
&\boldsymbol{\mu}(T,\mathbf{x})=\mathbf{0}, \quad \text{in } \Omega\\
&\boldsymbol{\mu}=-\tfrac{\partial B}{\partial p}\mathbf{n}, \quad \text{on } \Sigma_D\\
&[-v\mathbf{I}+\eta(\nabla\boldsymbol{\mu}+\nabla\boldsymbol{\mu}^{\mathrm{T}})]\mathbf{n}=-\rho(\mathbf{u}\cdot\mathbf{n})\boldsymbol{\mu}-\beta_1\tfrac{\partial A}{\partial\nabla\mathbf{u}}\mathbf{n}-\beta_2\tfrac{\partial B}{\partial\mathbf{u}}, \quad \text{on } \Sigma_N
\end{aligned}
\tag{13}
$$

The transient adjoint Eqs. (13) are terminal value problems, where the value of $\boldsymbol{\mu}$ at the terminal time T is specified and the transient solver is implemented from time T to 0. According to Eq. (12), the adjoint derivatives can be expressed as follows (see Appendix B for more details):

$$
\begin{aligned}
&\widehat{\left.\frac{DJ}{D\gamma}\right|}_{\Omega}=\int_0^T\beta_1\left(\tfrac{\partial A}{\partial\gamma}-\tfrac{\partial\alpha}{\partial\gamma}\mathbf{u}\cdot\boldsymbol{\mu}\right)\mathrm{d}t, \quad \text{in } \Omega\\
&\widehat{\left.\frac{DJ}{D\gamma}\right|}_{\partial\Omega}=\int_0^T\beta_2\tfrac{\partial B}{\partial\gamma}\mathrm{d}t, \quad \text{on } \partial\Omega
\end{aligned}
\tag{14}
$$

4. Numerical implementation of optimization problem

The topology optimization for unsteady Navier–Stokes flows is implemented using the gradient based iterative method. The procedure for an iterative optimization includes the following steps (Fig. 1): (a) the Navier–Stokes equations are solved with the given value of the design variable; (b) the adjoint equations are solved based on the numerical solution of the

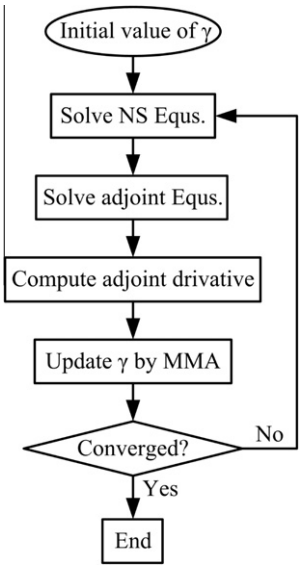

Fig. 1. The flowchart of the iterative optimization.

Navier–Stokes equations; (c) the adjoint derivatives of the objective function are computed by Eq. (14), and the adjoint derivatives of the design constraint are computed by a similar procedure; (d) the design variable is updated by the method of moving asymptotes (MMA) [53]. The above steps are implemented iteratively until the stopping criteria are satisfied. In the above procedure, the transient Navier–Stokes equations and the corresponding adjoint equations are solved by the finite element method using the commercial finite element software *Comsol Multiphysics* (Version 3.5) [52], where all the numerical implementation is merely based on the software's basic module: *COMSOL Multiphysics → PDE Modes → PDE, General Form*. The PDE modes of *Comsol Multiphysics* can solve partial differential equations of the form

$$\begin{aligned} &\mathbf{d}_a \tfrac{\partial \mathbf{u}}{\partial t} + \nabla \cdot \mathbf{\Gamma} = \mathbf{F}, \quad \text{in } Q \\ &-\mathbf{n} \cdot \mathbf{\Gamma} = \mathbf{G} + \left(\tfrac{\partial \mathbf{R}}{\partial \mathbf{u}}\right)^{\mathrm{T}} \boldsymbol{\lambda}, \quad \mathbf{R} = \mathbf{0}, \quad \text{on } \Sigma \end{aligned} \tag{15}$$

where $\mathbf{d}_a$ and $\mathbf{\Gamma}$ are matrixes; $\mathbf{F}$, $\mathbf{G}$ and $\mathbf{R}$ are vectors; $\mathbf{n}$ is the unit outward normal vector; $\Sigma = \Sigma_D \cup \Sigma_N$. For the 2D case, the transient Navier–Stokes equations can be solved by setting

$$\begin{aligned} &\mathbf{d}_a = \begin{pmatrix} \rho & 0 \\ 0 & \rho \\ 0 & 0 \end{pmatrix}; \quad \mathbf{\Gamma} = \begin{pmatrix} -2\eta \frac{\partial u_1}{\partial x} + p & -\eta\left(\frac{\partial u_1}{\partial y} + \frac{\partial u_2}{\partial x}\right) \\ -\eta\left(\frac{\partial u_1}{\partial y} + \frac{\partial u_2}{\partial x}\right) & -2\eta \frac{\partial u_2}{\partial y} + p \\ 0 & 0 \end{pmatrix}; \quad \mathbf{F} = \begin{pmatrix} -\alpha u_1 - \rho\left(u_1 \frac{\partial u_1}{\partial x} + u_2 \frac{\partial u_1}{\partial y}\right) \\ -\alpha u_2 - \rho\left(u_1 \frac{\partial u_2}{\partial x} + u_2 \frac{\partial u_2}{\partial y}\right) \\ -\left(\frac{\partial u_1}{\partial x} + \frac{\partial u_2}{\partial y}\right) \end{pmatrix} \\ &\mathbf{R} = \begin{pmatrix} u_1 - u_{1D} \\ u_2 - u_{2D} \\ 0 \end{pmatrix} \text{ on } \Sigma_D; \quad \mathbf{G} = \begin{pmatrix} 0 \\ 0 \\ 0 \end{pmatrix} \text{ on } \Sigma_D; \quad \mathbf{R} = \begin{pmatrix} 0 \\ 0 \\ 0 \end{pmatrix} \text{ on } \Sigma_N; \quad \mathbf{G} = \begin{pmatrix} g_1 \\ g_2 \\ 0 \end{pmatrix} \text{ on } \Sigma_N \end{aligned} \tag{16}$$

where $\mathbf{u} = (u_1, u_2)$, $\mathbf{u}_D = (u_{1D}, u_{2D})$ and $\mathbf{g} = (g_1, g_2)$. Similarly, the adjoint equations can be solved by setting

$$\begin{aligned} &\mathbf{d}_a = \begin{pmatrix} -\rho & 0 \\ 0 & -\rho \\ 0 & 0 \end{pmatrix}; \quad \mathbf{\Gamma} = \begin{pmatrix} -2\eta \frac{\partial \mu_1}{\partial x} - \beta_1 \frac{\partial A}{\partial u_{1x}} + v & -\eta\left(\frac{\partial \mu_1}{\partial y} + \frac{\partial \mu_2}{\partial x}\right) - \beta_1 \frac{\partial A}{\partial u_{1y}} \\ -\eta\left(\frac{\partial \mu_1}{\partial y} + \frac{\partial \mu_2}{\partial x}\right) - \beta_1 \frac{\partial A}{\partial u_{2x}} & -2\eta \frac{\partial \mu_2}{\partial y} - \beta_1 \frac{\partial A}{\partial u_{2y}} + v \\ 0 & 0 \end{pmatrix} \\ &\mathbf{F} = \begin{pmatrix} -\alpha\mu_1 - \beta_1 \frac{\partial A}{\partial u_1} + \rho\left(u_1 \frac{\partial \mu_1}{\partial x} + u_2 \frac{\partial \mu_1}{\partial y} - \mu_1 \frac{\partial u_1}{\partial x} - \mu_2 \frac{\partial u_1}{\partial y}\right) \\ -\alpha\mu_2 - \beta_1 \frac{\partial A}{\partial u_2} + \rho\left(u_1 \frac{\partial \mu_2}{\partial x} + u_2 \frac{\partial \mu_2}{\partial y} - \mu_1 \frac{\partial u_2}{\partial x} - \mu_2 \frac{\partial u_2}{\partial y}\right) \\ \beta_1 \frac{\partial A}{\partial p} - \left(\frac{\partial \mu_1}{\partial x} + \frac{\partial \mu_2}{\partial y}\right) \end{pmatrix}; \quad \mathbf{R} = \begin{pmatrix} \mu_1 + n_1 \frac{\partial B}{\partial p} \\ \mu_2 + n_2 \frac{\partial B}{\partial p} \\ 0 \end{pmatrix} \text{ on } \Sigma_D; \quad \mathbf{G} = \begin{pmatrix} 0 \\ 0 \\ 0 \end{pmatrix} \text{ on } \Sigma_D \\ &\mathbf{R} = \begin{pmatrix} 0 \\ 0 \\ 0 \end{pmatrix} \text{ on } \Sigma_N; \quad \mathbf{G} = \begin{pmatrix} -\rho\mu_1(u_1 n_1 + u_2 n_2) - \beta_1\left(n_1 \frac{\partial A}{\partial u_{1x}} + n_2 \frac{\partial A}{\partial u_{1y}}\right) - \beta_2 \frac{\partial B}{\partial u_1} \\ -\rho\mu_2(u_1 n_1 + u_2 n_2) - \beta_1\left(n_1 \frac{\partial A}{\partial u_{2x}} + n_2 \frac{\partial A}{\partial u_{2y}}\right) - \beta_2 \frac{\partial B}{\partial u_2} \\ 0 \end{pmatrix} \text{ on } \Sigma_N \end{aligned} \tag{17}$$

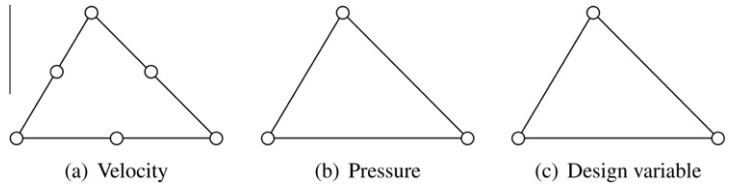

Fig. 2. The finite element nodes used to express the velocity, pressure and design variable on a triangular element.

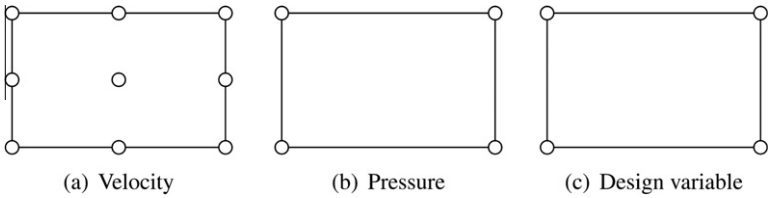

Fig. 3. The finite element nodes used to express the velocity, pressure and design variable on a rectangular element.

where $\boldsymbol{\mu} = (\mu_1, \mu_2)$ and $\mathbf{n} = (n_1, n_2)$. The numerical integrations in the time domain are implemented by solving a scalar general form equation (Eq. (18)) in *Comsol*

$$\begin{aligned} &d_a \tfrac{\partial u}{\partial t} + \nabla \cdot \Gamma = F, \quad \text{in } Q \\ &-\mathbf{n} \cdot \Gamma = G + \left(\tfrac{\partial R}{\partial u}\right)^{\mathrm{T}} \lambda, \quad R = 0, \quad \text{on } \Sigma \end{aligned} \tag{18}$$

By setting

$$d_a = 1, \quad \Gamma = \mathbf{0}, \quad G = 0, \quad R = 0, \quad F = \beta_1 \left(\frac{\partial A}{\partial \gamma} - \frac{\partial \alpha}{\partial \gamma} \mathbf{u} \cdot \boldsymbol{\mu} \right) \tag{19}$$

and solving Eq. (18) for u, the adjoint derivative $\widehat{\frac{DJ}{D\gamma}}\Big|_{\Omega}$ in Eq. (14) can be obtained as $u|_{t=T}$. Changing the value of F in Eq. (19) to $\beta_2 \frac{\partial B}{\partial \gamma}$, the adjoint derivative $\widehat{\frac{DJ}{D\gamma}}\Big|_{\partial\Omega}$ can be solved as $u|_{\partial\Omega, t=T}$. The spatial integrations in the iterative procedure can be performed by the inner function *postint* of *Comsol*. For the 3D case, the settings for Eqs. (15) and (18) are similar to the 2D case. During the optimization procedure, the Navier–Stokes equations and the adjoint equations are solved using Taylor–Hood elements [54], which interpolate the fluidic velocity quadratically and the pressure linearly. The design variable is interpolated linearly based on the corner nodes of the elements (Figs. 2 and 3). The transient equations are solved using the backward differentiation formula method, choosing *BDF* for the time dependent solver *femtime* of *Comsol* [55]. In this paper, the stopping criteria are specified as the change of values of the objective between two consecutive iterations and the residual of the volume constraint satisfying

$$\begin{aligned} &|J_k - J_{k-1}|/|J_0| < 1 \times 10^{-6} \\ &\left| \textstyle\int_\Omega \gamma d\Omega / V_0 - \theta \right| / \theta < 1 \times 10^{-3} \end{aligned} \tag{20}$$

The authors note that *Comsol* is a convenient software program for implementing transient optimization problems when the continuous adjoint method is adopted.

5. Numerical examples

In this section, several numerical examples are presented to demonstrate the capability and utility of the proposed topology optimization method for unsteady Navier–Stokes flows. The density and viscosity of the fluid are set as 1, if there is no specification. The values of α_{max} and q are chosen based on numerical experiments. More details are available in [23]. The Reynolds number is calculated as

$$\mathrm{Re} = \rho U_{max} L / \eta \tag{21}$$

where L is the width of the inlet, and U_{max} is the maximal value of the velocity on the inlet. The initial value condition of the transient Navier–Stokes equations is $\mathbf{u}_0 = \mathbf{0}$. The objective function for the topology optimization problem in Eq. (7) is chosen as the energy dissipation inside the design domain and the pressure on the inlet as

$$J(\mathbf{u}, p; \gamma) = \int_0^T \int_\Omega \beta_1 \left[\frac{\eta}{2} (\nabla \mathbf{u} + \nabla \mathbf{u}^{\mathrm{T}}) : (\nabla \mathbf{u} + \nabla \mathbf{u}^{\mathrm{T}}) + \alpha \mathbf{u}^2 \right] \mathrm{d}\Omega \mathrm{d}t + \int_0^T \int_{\Gamma_i} \beta_2 p \, \mathrm{d}\Gamma \mathrm{d}t \tag{22}$$

where Γ_i is the boundary of the inlet. The parameters β_1 and β_2 depend on specified examples and can be adjusted by the designer based on design necessity or numerical experiments.

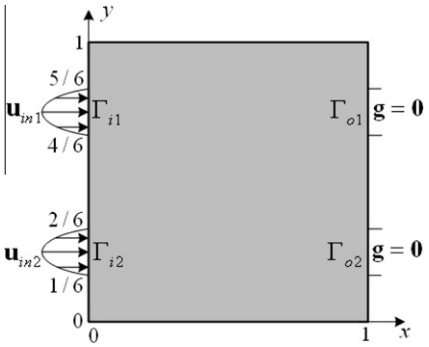

Fig. 4. Design domain of the double pipe. The values $\mathbf{u}_{in1}$ and $\mathbf{u}_{in2}$ are the velocity distribution on the inlets.

Table 1
Parameter settings in the topology optimization of a double pipe.

β_1	β_2	θ	α_{min}	α_{max}	q
1	0	1/3	0	1×10^4	1

Fig. 5. Optimal design of the double pipe for unsteady Navier–Stokes flows corresponding to the inlet velocity in Eq. (23).

5.1. Double pipe

A double pipe is used to investigate the feasibility of the proposed optimization method. The design domain is shown in Fig. 4 and is discretized by 60×60 rectangular elements. The optimization parameter values are shown in Table 1. The Neumann boundary condition in Eq. (4) is loaded on the outlets Γ_{o1} and Γ_{o2} by setting $\mathbf{g} = \mathbf{0}$. When the transient velocity in Eq. (23)

$$\begin{aligned} \mathbf{u}_{in1} &= -144(y - 4/6)(5/6 - y)\cos(t)\mathbf{n}, \quad t \in [0, 2\pi] \\ \mathbf{u}_{in2} &= -144(y - 1/6)(2/6 - y)\sin(t)\mathbf{n}, \quad t \in [0, 2\pi] \end{aligned} \tag{23}$$

is imposed on the inlets, the optimized result is shown in Fig. 5. Snapshots of the optimization procedure are shown in Fig. 6. The convergent history of the value of the objective and the volume of the fluidic channel is shown in Fig. 7. Snapshots of the streamline of the unsteady flow at specific points in time are shown in Fig. 8.

By solving the topology optimization of the double pipe example for the steady case, instead of the transient case, one can obtain the optimized channels in Fig. 9a when the injecting velocity in Eq. (24) is imposed on the inlets

$$\begin{aligned} \mathbf{u}_{in1} &= -144(y - 4/6)(5/6 - y)\mathbf{n} \\ \mathbf{u}_{in2} &= -144(y - 1/6)(2/6 - y)\mathbf{n} \end{aligned} \tag{24}$$

The optimized result in Fig. 9a agrees with the numerical results shown by Borrvall and Petersson in [12] for steady flows. By changing $\mathbf{u}_{in2}$ to be a velocity of suction and maintaining $\mathbf{u}_{in1}$ a velocity of injection (Eq. (25)),

$$\begin{aligned} \mathbf{u}_{in1} &= -144(y - 4/6)(5/6 - y)\mathbf{n} \\ \mathbf{u}_{in2} &= 144(y - 1/6)(2/6 - y)\mathbf{n} \end{aligned} \tag{25}$$

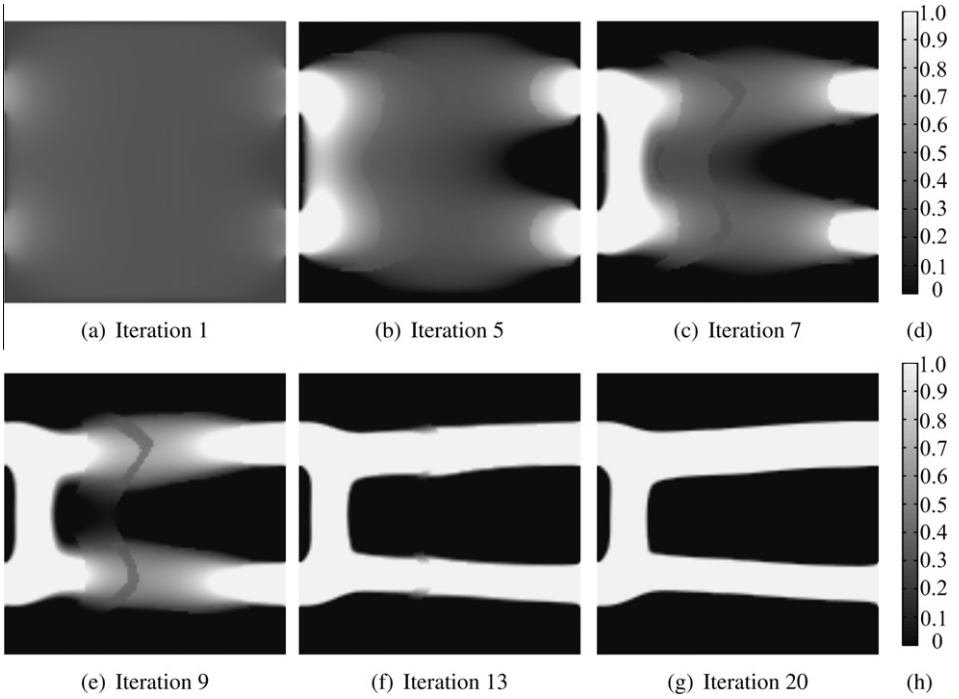

Fig. 6. Snapshots of optimization procedure for double pipe example in Fig. 5.

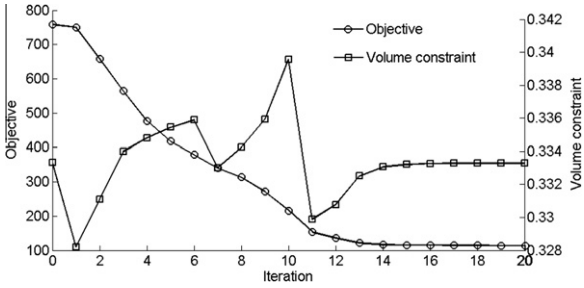

Fig. 7. Convergent history of the objective and volume constraint for the optimal design shown in Fig. 5.

a bend pipe is obtained as shown in Fig. 9(b), where the fluid flows from Γ_{i1} to Γ_{i2} directly. When both $\mathbf{u}_{in1}$ and $\mathbf{u}_{in2}$ are velocities of suction (Eq. (26)),

$$\begin{aligned}\mathbf{u}_{in1} &= 144(y-4/6)(5/6-y)\mathbf{n}\\ \mathbf{u}_{in2} &= 144(y-1/6)(2/6-y)\mathbf{n}\end{aligned} \tag{26}$$

the optimized channel is shown in Fig. 9(c). Fig. 9(a)–(c) show that the optimal design is a double pipe when $\mathbf{u}_{in1}$ and $\mathbf{u}_{in2}$ are both the velocity of injection or suction, and the optimal design is a bend channel when $\mathbf{u}_{in1}$ and $\mathbf{u}_{in2}$ are the velocity of suction and injection respectively. According to Eq. (23), $\mathbf{u}_{in1}$ and $\mathbf{u}_{in2}$ are the velocity of injection as $t \in (0,\pi/2)$; the velocity of suction and injection as $t \in (\pi/2,\pi)$; the velocity of suction as $t \in (\pi,3\pi/2)$; and the velocity of injection and suction as $t \in (3\pi/2,2\pi)$. Therefore, the fluid could be transported between Γ_{i1} and Γ_{i2} as $t \in (\pi/2,\pi) \cup (3\pi/2,2\pi)$ and could flow in parallel between the inlets and outlets as $t \in (0,\pi/2) \cup (\pi,3\pi/2)$. This analysis is consistent with the streamline distribution in Fig. 8. By imposing the velocity of inlet in Eqs. (23)–(26) for the optimized results in Figs. 5 and 9 respectively, the values of the objective in Eq. (22) shown in Table 2 can be obtained. By cross comparison the data in Table 2 and the optimized channels in Figs. 5 and 9, one can conclude that the optimal topology of a channel is valid only corresponding to the specific inlet velocity that is specified during the optimization procedure. Therefore, it is reasonable that the optimal topology for unsteady flow is different from its steady counterparts.

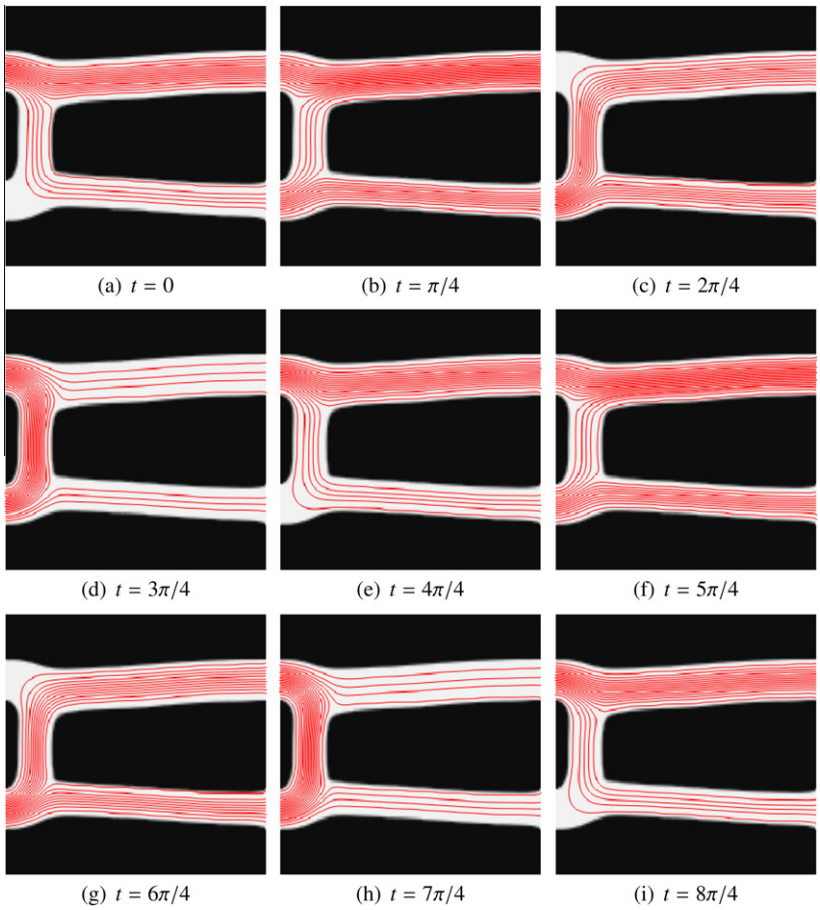

Fig. 8. Streamline snapshots of the unsteady double pipe flow corresponding to the optimal design in Fig. 5.

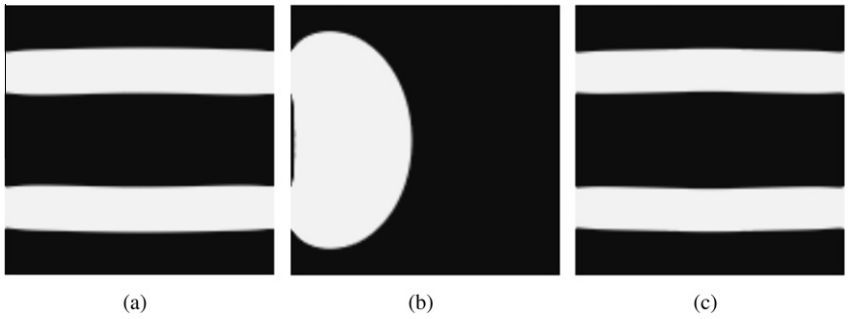

Fig. 9. Optimal designs of the double pipe for steady Navier–Stokes flows corresponding to the inlet velocity in Eqs. (24)–(26), respectively.

The dynamic effects of inflow can be adjusted by tuning the parameter ϖ in Eq. (27)

$$\begin{aligned}\mathbf{u}_{in1} &= -144(y-4/6)(5/6-y)\cos(\varpi t)\mathbf{n}\\ \mathbf{u}_{in2} &= -144(y-1/6)(2/6-y)\sin(\varpi t)\mathbf{n}\end{aligned} \tag{27}$$

A larger value of ϖ corresponds to an obvious oscillation of inflow. Fig. 10 shows the optimized double pipes for different values of ϖ. These results illustrate the need to implement optimization of unsteady flow.

5.2. Three-terminal device

Fluidic channels with periodic dynamic input on the inlet have been widely used in fluidic devices [56]. In this example, a three-terminal device with periodic transient velocity on the inlet Γ_i, given as the equation

$$\mathbf{u}_{in} = -1\times 10^4(y-1)(1.2-y)\sin(t)\mathbf{n} \tag{28}$$

Table 2
Objective values of the double pipe in the optimal designs of Figs. 5 and 9, where J_U, J_{Sa}, J_{Sb} and J_{Sc} are the objective values obtained by imposing the velocity in Eqs. (23)–(26) on the inlets of the optimal designs in Figs. 5 and 9, respectively.

	Eq. 23	Eq. 24	Eq. 25	Eq. 26
J_U	113.8	56.65	16.14	56.65
J_{Sa}	133.6	48.60	37.08	48.73
J_{Sb}	606.6	379.8	6.04	379.8
J_{Sc}	134.8	48.78	48.73	48.71

Fig. 10. Optimal designs of the double pipe corresponding to different values of ϖ in Eq. (27).

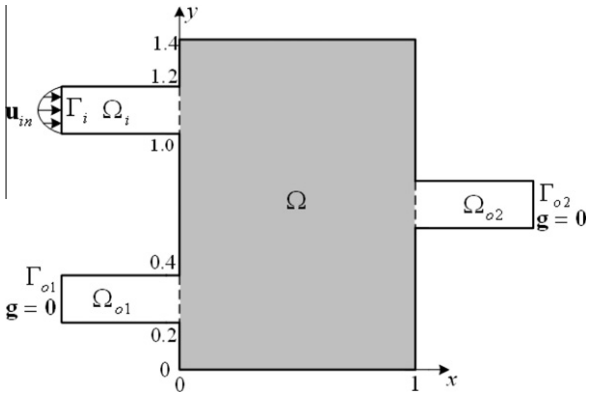

Fig. 11. Design domain of the three-terminal device. The value $\mathbf{u}_{in}$ is the velocity distribution on the inlet.

is optimized. According to Eq. (21), the Reynolds number is 100 in this example. The design domain Ω is shown in Fig. 11, where the inlet duct is Ω_i and the outlet ducts are Ω_{o1} and Ω_{o2}. The design domain is discretized by 100×140 rectangular elements. The Neumann boundary condition in Eq. (4) is loaded on the outlets Γ_{o1} and Γ_{o2} by setting $\mathbf{g} = \mathbf{0}$. The other boundaries are set as no-slip boundaries. Three time intervals $[0,\pi]$, $[\pi,2\pi]$ and $[0,2\pi]$ which correspond to pure injection flow, pure suction flow and periodic injection-suction flow, are considered separately. The optimization parameter values are shown in Table 3 and the optimal topologies of the device are shown in Fig. 12(a)–(c). Fig. 13 shows the optimized device where the steady velocity condition is loaded on the inlet Γ_i as

$$\mathbf{u}_{in} = -1 \times 10^4 (y-1)(1.2-y)\mathbf{n} \tag{29}$$

From Fig. 12, one can see that the suction flow occurring as $t \in (\pi, 2\pi)$ is a key point in the difference of the shape of the device compared to the steady flow case. By imposing the velocity boundary in Eqs. (28) and (29) on the inlets of the optimal designs in Figs. 12 and 13 respectively, the values of objective listed in Table 4 can be obtained. The cross comparison of the values of energy dissipation confirms further that the dynamic effect of the unsteady flow can influence the detailed shape of the device. This example illustrates that the optimal design of a unsteady flow is influenced by the dynamic effect induced by the different choice of time intervals.

5.3. A bend channel

An example of a bend channel with different Reynolds numbers under steady flow has been discussed by Gersborg-Hansen et al. in [22]. A similar example is discussed here for unsteady flows. The computational domain includes the inlet

Table 3
Parameter settings in the topology optimization of three-terminal device.

β_1	β_2	θ	α_{min}	α_{max}	q
1	0	0.3	0	1×10^4	1

Fig. 12. Optimal designs of the three-terminal device. Here, (a), (b) and (c) are optimal designs for unsteady flows corresponding to the time intervals $[0,\pi]$, $[\pi,2\pi]$ and $[0,2\pi]$, respectively.

Fig. 13. Optimal design of the three-terminal device for steady flow.

Table 4
Objective values of the optimal designs in Figs. 12 and 13. J_{Ta}, J_{Tb}, J_{Tc} and J_S are objective values obtained by imposing the velocity in Eqs. (28) and (29) on the inlets of optimal designs in Figs. 12 and 13.

	Steady	$t \in [0,\pi]$	$t \in [\pi,2\pi]$	$t \in [0,2\pi]$
J_{Ta}	1.064×10^5	1.298×10^5	1.305×10^5	2.605×10^5
J_{Tb}	1.347×10^5	1.579×10^5	1.258×10^5	2.841×10^5
J_{Tc}	1.138×10^5	1.302×10^5	1.271×10^5	2.574×10^5
J_S	1.062×10^5	1.299×10^5	1.300×10^5	2.602×10^5

duct Ω_i, the outlet duct Ω_o and the design domain Ω (Fig. 14), which are discretized by 40×20, 40×20 and 100×100 rectangular elements respectively. The transient velocity is set as

$$\mathbf{u}_{in} = -4U_{max}(y - 3.5)(4.5 - y)t\mathbf{n}, \quad t \in [0,1] \tag{30}$$

where U_{max} is specified as 1, 50 and 300, which corresponds to the Reynolds numbers of 1, 50 and 300 respectively. The optimization parameter values are shown in Table 5. The optimized channels corresponding to different Reynolds numbers and the corresponding values of the objective are shown in Fig. 15 and Table 6. The results in Fig. 15 show that the bend channel has sharp corners for flow with low Reynolds number, and the corners become rounder for a larger Reynolds number. Therefore, the optimized channel is relatively straight for a flow with a low Reynolds number, and develops bending for a flow with a larger Reynolds number. The results agree with those obtained by Gersborg-Hansen et al. in [22] for steady flows.

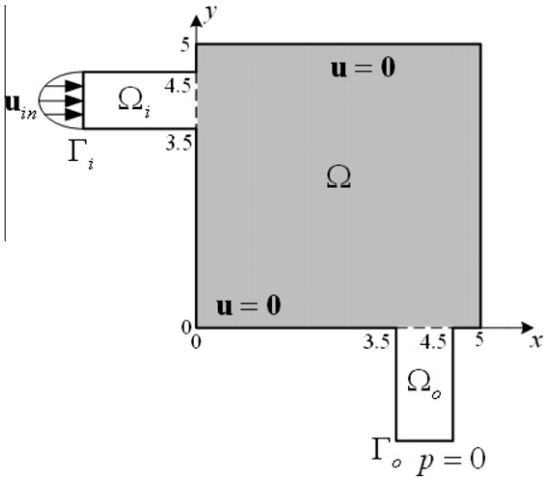

Fig. 14. Design domain of the bend channel. The value $\mathbf{u}_{in}$ is the velocity distribution on the inlet.

Table 5
Parameter settings in the topology optimization of a bend channel.

β_1	β_2	θ	α_{min}	α_{max}	q
1	0.1	0.25	0	1×10^4	1

(a) Re=1 (b) Re=50 (c) Re=300

Fig. 15. Optimal designs of the bend channel corresponding to different Reynolds numbers.

5.4. Target flux on outlet

The flow rate on the outlet is an important factor for fluidic devices [56,57]. The target flux on the outlet can be produced by adding a flux constraint on the outlet of the design domain. According to the flow rate constraint for optimization of steady flows [19,58], the target flux for a unsteady flow is added into the topology optimization problem in Eq. (7) as an inequality constraint

$$\left(\frac{\int_{T_1}^{T_2}\int_{\Gamma_o}\mathbf{u}\cdot\mathbf{n}\,\mathrm{d}\Gamma\mathrm{d}t}{Q_{tar}}-1\right)^2\leqslant\epsilon \tag{31}$$

where $[T_1,T_2]\subseteq[0,T]$ is the time interval; Γ_o is the outlet boundary; Q_{tar} is the target flux on the corresponding outlet; and ϵ is the allowable tolerance. The adjoint analysis for the flux constraint follows the same procedure as that for the objective in Section 3. Additionally, the objective or certain design constraints may be defined on the subinterval $[T_1,T_2]\subseteq[0,T]$, while the others are still defined on the whole time interval $[0,T]$. Therefore, the adjoint analysis of the corresponding expression will be implemented on $[0,T_2]$ instead of $[0,T]$, although the unsteady flow problem is defined on the whole time interval $[0,T]$. Accordingly, the corresponding adjoint equations and adjoint derivatives are transient equations and integrations on $[0,T_2]$ instead of $[0,T]$, respectively (see Appendix C for more details).

Table 6
Objective values of the optimal designs in Fig. 15.

	Re = 1	Re = 50	Re = 300
J	2.094×10^1	5.722×10^4	2.745×10^6

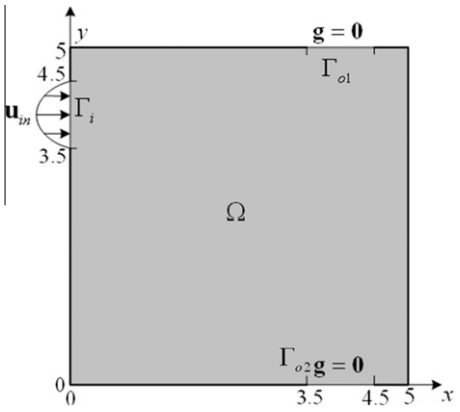

Fig. 16. Design domain of the flux distribution device.

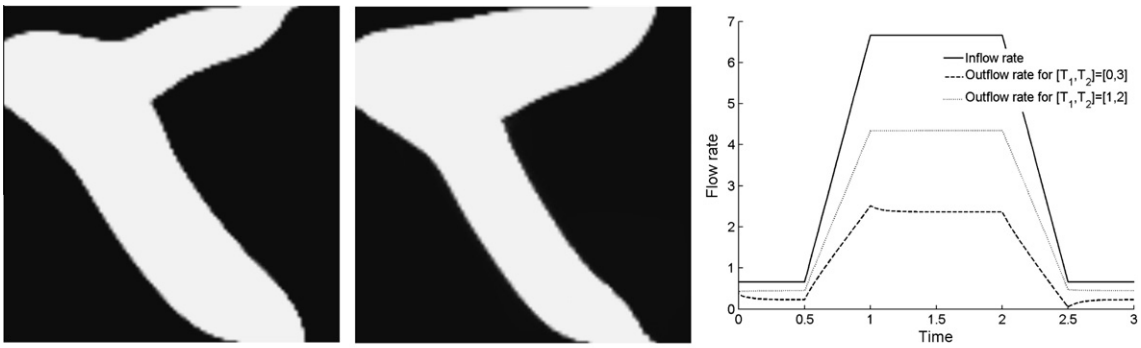

Fig. 17. (a) Optimal design of the flux distribution device with flux constraint defined on the whole time interval [0,3]; (b) optimal design of the flux distribution device with flux constraint defined on the time interval [1,2]; (c) the absolute inflow rate over time on the inlet Γ_i and the outflow rate over time on the outlet Γ_{o1}.

First, a flux distribution device is optimized. The design domain is shown in Fig. 16a, and is discretized by 100×100 rectangular elements. The velocity loaded on the inlet is (Fig. 17c)

$$\begin{aligned}\mathbf{u}_{in} = -[&4(y-3.5)(4.5-y)(t \leqslant 0.5) + 4(y-3.5)(4.5-y)(18t-8)(0.5 < t \leqslant 1) + 40(y-3.5)(4.5-y)(1 < t \leqslant 2)\\ &+ 4(y-3.5)(4.5-y)(-18t+46)(2 < t \leqslant 2.5) + 4(y-3.5)(4.5-y)(t > 2.5)]\mathbf{n}, \quad t \in [0,3]\end{aligned} \tag{32}$$

The optimization parameter values are shown in Table 7. The flux constraint with the formulation as Eq. (31) is imposed on the outlet Γ_{o1} to constrain the flux distribution between the two outlets Γ_{o1} and Γ_{o2}. The parameters in Eq. (31) are chosen to be 1×10^{-4} for ϵ and $\frac{1}{3}\int_0^3 \int_{\Gamma_i} -\mathbf{u}_{in} \cdot \mathbf{n}\, d\Gamma dt$ for Q_{tar}. When $[T_1, T_2]$ is set equal to $[0, T]$, the design constraint is

$$\left(\frac{\int_0^3 \int_{\Gamma_{o1}} \mathbf{u} \cdot \mathbf{n} d\Gamma dt}{\frac{1}{3}\int_0^3 \int_{\Gamma_i} -\mathbf{u}_{in} \cdot \mathbf{n}\, d\Gamma dt} - 1\right)^2 \leqslant 1 \times 10^{-4} \tag{33}$$

Then the objective and the design constraint are both defined on the whole time interval. The optimized flux distribution device is shown in Fig. 17(a). The objective value corresponding to the result in Fig. 17(a) is 1.740×10^3. When the time interval $[T_1, T_2]$ is set to be $[1,2]$, the design constraint is modified as

$$\left(\frac{\int_1^2 \int_{\Gamma_{o1}} \mathbf{u} \cdot \mathbf{n}\, d\Gamma dt}{\frac{1}{3}\int_0^3 \int_{\Gamma_i} -\mathbf{u}_{in} \cdot \mathbf{n}\, d\Gamma dt} - 1\right)^2 \leqslant 1 \times 10^{-4} \tag{34}$$

Table 7
Parameter settings in the topology optimization of a device with target flux on the outlet.

β_1	β_2	θ	α_{min}	α_{max}	q
1	0	0.4	0	1×10^3	1

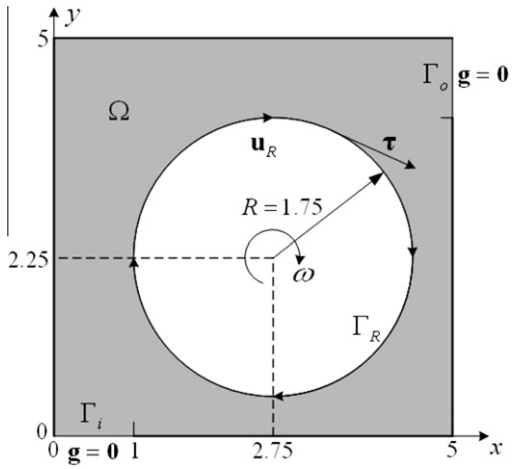

Fig. 18. Design domain of the roller-type pump.

Table 8
Parameter settings in the topology optimization of a roller-type pump.

β_1	β_2	θ	α_{min}	α_{max}	q
1	0	0.4	0	1×10^3	1

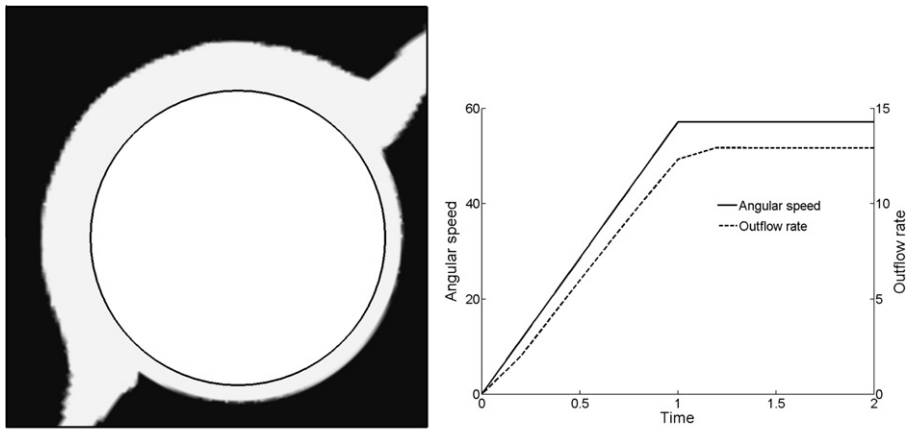

Fig. 19. (a) Optimal design of the roller-type pump; (b) the angular velocity over time and the outflow rate over time on the outlet Γ_o.

and the objective is still defined on the whole time interval. According to the derivation of adjoint sensitivity in Appendix C, the adjoint equations and sensitivity corresponding to the flux constraint are defined on the time interval [0,2]. By keeping the other parameters unchanged, the optimization problem is solved. The optimized result is shown in Fig. 17b. The value of the objective corresponding to the result in Fig. 17b is 1.257×10^3. The outflow rate on the outlet Γ_{o1} corresponding to the above two optimal designs is shown in Fig. 17c. Because the fluid considered in this paper is incompressible, the left fluid must flow out from the outlet Γ_{o2} when the target flux constraint is satisfied on the outlet Γ_{o1}. Therefore, the optimized channels in Fig. 17a and b have two branches. The flux constraints in Eqs. (33) and (34) mean that the flux at the outlet

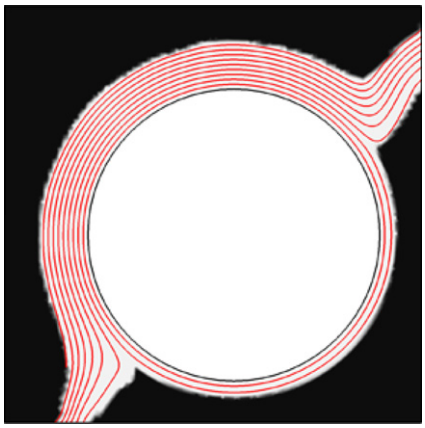

Fig. 20. Streamlines of the flow in the optimal design of the roller-type pump at $t = 0.8$.

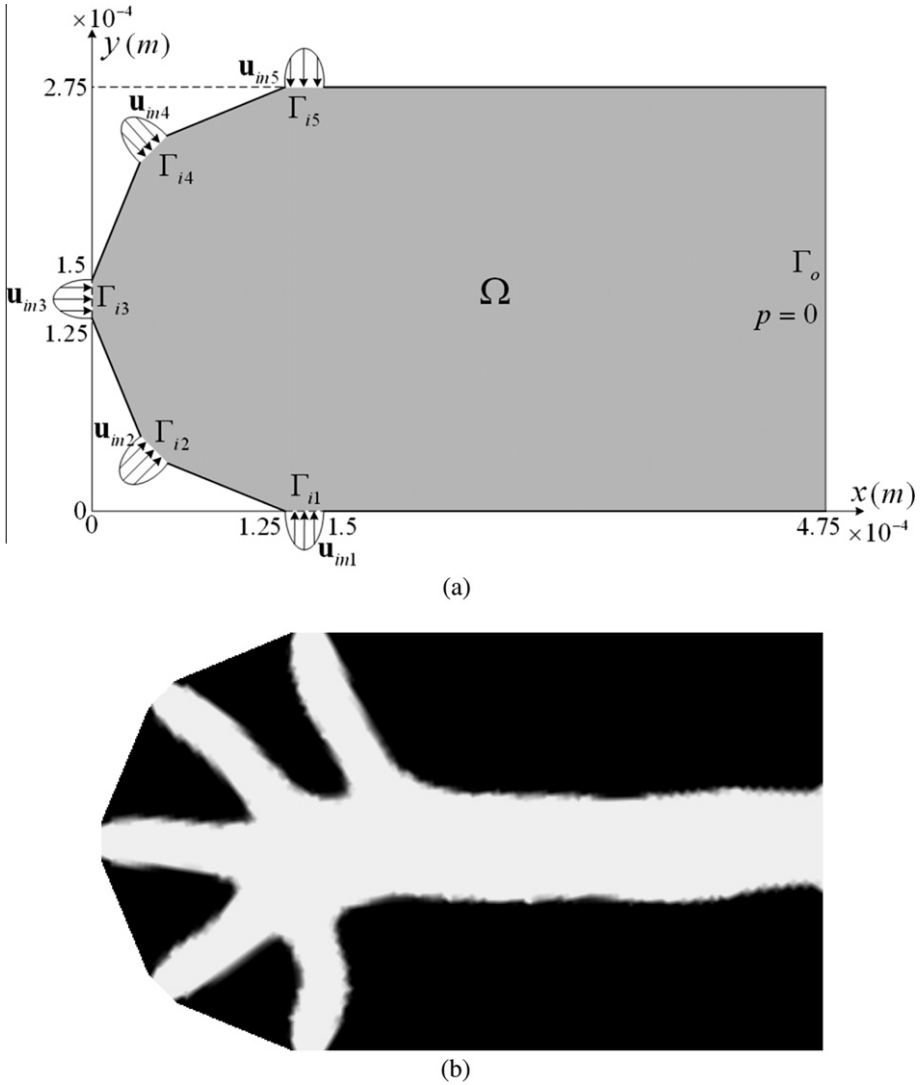

Fig. 21. (a) Design domain of the star-shaped microchannel chip; (b) optimal design of the star-shaped microchannel chip.

Table 9
Parameter settings in the topology optimization of a star-shaped microchannel chip.

β_1	β_2	θ	α_{min}	α_{max}	q
1	0.1	0.35	0	1×10^6	1

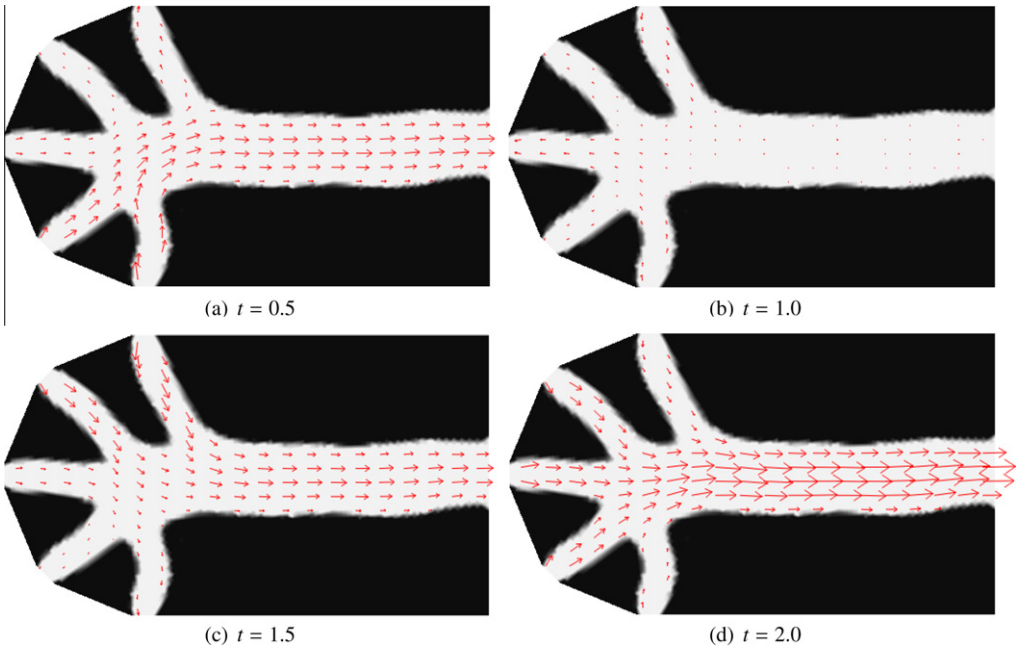

Fig. 22. Snapshots of the distribution of fluidic velocity.

Γ_{o1} of the optimal design in Fig. 17(a) is lower than that in Fig. 17(b). Therefore, the thick branch connected to Γ_{o1} in Fig. 17(b) is helpful for decreasing the velocity gradient and dissipation of the flow.

Second, a roller-type pump, which pumps the liquid using a rotating roller, is optimized. Fig. 18 shows the design domain, where the rotating roller drives the liquid flowing from the inlet Γ_i to the outlet Γ_o. The fluidic velocity on the surface of the roller is equal to the rotational velocity of the roller surface,

$$\mathbf{u}_r = \omega(t) R \boldsymbol{\tau}, \quad t \in [0, 2] \tag{35}$$

where $\omega(t)$ is the transient angular speed of the roller; R is the radius of the roller; and $\boldsymbol{\tau}$ is the unit tangential vector of the roller surface. The optimization parameter values are shown in Table 8. By setting Q_{tar} and ϵ to 20 and 1×10^{-4} respectively, the flux constraint shown in Eq. (31) is imposed on the boundary Γ_o as

$$\left(\frac{\int_0^2 \int_{\Gamma_o} \mathbf{u} \cdot \mathbf{n} \mathrm{d}\Gamma \mathrm{d}t}{20} - 1 \right)^2 \leqslant 1 \times 10^{-4} \tag{36}$$

The design domain is discretized by 171519 triangular elements. After the transient angular speed is set to $\omega(t) = 400\min(t, 1)/7$ (Fig. 19(b)), the optimized roller-type pump is shown in Fig. 19(a). The objective value corresponding to the result in Fig. 19(a) is 5.866×10^5. The outflow rate over time is shown in Fig. 19(b). The streamline distribution of the flow in the optimized pump is shown in Fig. 20. Fig. 20 shows that the streamlines near the surface of the pump's roller is closed, while the others start at the inlet and end at the outlet. Therefore, a net flux between the inlet and outlet of the pump is produced by the rotating roller.

5.5. Star-shaped microchannel chip

Lab-on-a-chip devices have been become a popular technique in biochemistry and bioengineering [59,60]. This example involves the design of an infuser, a device that feeds a reactor or a piece of analysis equipment with a specific amount of fluid [52]. Flushing the fluidic channel is an important step to maintain consistent performance and enhance the efficiency of an infuser. The fluid flowing through an infuser is water, with density and viscosity equal to 1×10^3 kg/m^3 and 1×10^{-3} Pa · s,

respectively. The design domain is shown in Fig. 21(a) and is discretized by 160866 triangular elements. The transient velocity loaded on the inlets of the Star-shaped microchannel is

$$\begin{aligned}
\mathbf{u}_{in1} &= -U(1+2\sin(\pi t))\mathbf{n}\\
\mathbf{u}_{in2} &= -U(1+2\sin(\pi t+\pi/4))\mathbf{n}\\
\mathbf{u}_{in3} &= -U(1+2\sin(\pi t+\pi/2))\mathbf{n}\\
\mathbf{u}_{in4} &= -U(1+2\sin(\pi t+3\pi/4))\mathbf{n}\\
\mathbf{u}_{in5} &= -U(1+2\sin(\pi t+\pi))\mathbf{n}
\end{aligned} \tag{37}$$

where $U = 4\times 10^{-2}\chi(1-\chi)$ is a parabolic distribution on the inlets of the design domain, and χ is the local coordinate on the corresponding inlet. The energy dissipation and pressure distribution at the inlet (Eq. (22)) are set as the objective. The time interval is chosen to be [0,2]. The optimization parameter values are shown in Table 9. The optimized infuser has star-shaped channels (Fig. 21(b)). The objective value corresponding to the result in Fig. 21(b) is 795.6. Snapshots for the distribution of the fluidic velocity are shown in Fig. 22. Fig. 22 shows that the fluid pulses through the star-shaped chip periodically. This periodic pulsing is helpful for the effective flushing of leftovers in the chip.

6. Conclusion

The topology optimization method has been successfully used to design the unsteady incompressible Navier–Stokes flows at low and moderate Reynolds numbers. This makes topology optimization more useful for practical engineering designs, such as a flow with unsteady state or optimization focusing on the dynamic effect of fluid. Based on the continuous adjoint method, the topology optimization problem of the unsteady Navier–Stokes flow has been analyzed, and the numerical optimization procedure can be implemented by user-available numerical computational methods, such as the finite difference method, the finite element method or the finite volume method. Several examples have been presented, and the corresponding results have demonstrated that the optimized design of the unsteady Navier–Stokes flow is influenced by the dynamic effect, the Reynolds number and the constraints on the flux of fluid.

Acknowledgments

This work was supported by the China National Science fund (No. 50975272), the China National High Technology Research and Development program (863 program) (No. 2007 AA 042102) and SKLAO open fund in CIOMP. The authors are grateful to Professor Krister Svanberg for supply of the Matlab codes of MMA.

Appendix A. Adjoint equations of unsteady incompressible Navier–Stokes equations

To analyze the transient Navier–Stokes equations for the topology optimization problem in Eq. (7), the functional spaces for variables are chosen to be

$$\begin{aligned}
&\mathbf{u}\in\mathbf{V}_\Omega := \mathbf{L}^2((0,T);\mathbf{H}^1(\Omega)); \quad p\in \mathrm{V}_\Omega := \mathrm{L}^2((0,T);\mathrm{L}^2(\Omega))\\
&\mathbf{f}\in\mathbf{V}^*_\Omega := \mathbf{L}^2((0,T);\mathbf{H}^*(\Omega)); \quad \mathbf{u}_0\in\mathbf{H}^1_0(\Omega); \quad \gamma\in\mathrm{L}^1(\Omega)
\end{aligned} \tag{A.1}$$

where $\mathbf{H}^1(\Omega) := (\mathrm{H}^1(\Omega))^d$; d is the spatial dimension; $\mathrm{L}^1(\Omega)$ and $\mathrm{L}^2(\Omega)$ are the first-order and second-order integrable Lebesgue spaces respectively; $\mathbf{H}^*(\Omega)$ is the dual space of the Hilbert space $\mathbf{H}^1(\Omega)$; and $\mathbf{H}^1_0(\Omega) = \{\mathbf{u}\in\mathbf{H}^1(\Omega)|\nabla\cdot\mathbf{u}=0\}$. According to the Rietz representation theorem and the Hölder inequality [61], it is known that the Bochner space V_Ω is reflexive, i.e., $\mathrm{V}^*_\Omega = \mathrm{V}_\Omega$. Based on the adjoint analysis method, the sensitivity analysis of the optimization problem in Eq. (7) can be derived as follows: Based on [51]

$$\left\langle u^*, \int_0^T f(t)\mathrm{d}t\right\rangle_{\mathrm{X}^*,\mathrm{X}} = \int_0^T \langle u^*, f(t)\rangle_{\mathrm{X}^*,\mathrm{X}}\mathrm{d}t \tag{A.2}$$

where X is a Bochner space, and its dual is X^*, $u^*\in\mathrm{X}^*$, f: $(0,T)\to\mathrm{X}$ is Bochner integrable, then the integration on time and on space can change sequence. Therefore,

$$\begin{aligned}
e(\mathbf{u},p;\gamma) = &\int_0^T\int_\Omega\left[\rho\frac{\partial\mathbf{u}}{\partial t} - \eta\nabla\cdot(\nabla\mathbf{u}+\nabla\mathbf{u}^{\mathrm{T}}) + \rho(\mathbf{u}\cdot\nabla)\mathbf{u} + \nabla p - \mathbf{f}\right]\cdot\mathbf{v}\ \mathrm{d}\Omega\mathrm{d}t - \int_0^T\int_\Omega q\nabla\cdot\mathbf{u}\ \mathrm{d}\Omega\mathrm{d}t\\
&+\int_0^T\int_{\Gamma_D}\mathbf{u}\cdot\mathbf{v}\ \mathrm{d}\Gamma\mathrm{d}t + \int_0^T\int_{\Gamma_N}\left[-p\mathbf{I}+\eta(\nabla\mathbf{u}+\nabla\mathbf{u}^{\mathrm{T}})\right]\mathbf{n}\cdot\mathbf{v}\ \mathrm{d}\Gamma\mathrm{d}t + \int_\Omega(\mathbf{u}\cdot\mathbf{v})\Big|_{t=0}\mathrm{d}\Omega
\end{aligned} \tag{A.3}$$

for $\forall \mathbf{v} \in \mathbf{V}_\Omega$ and $\forall q \in \mathrm{V}_\Omega$. Based on Eq. (A.2), the following transformation of Eq. (A.3) is obtained by partial integration on time:

$$\begin{aligned} e(\mathbf{u},p;\gamma) = {} & \rho \int_\Omega \int_0^T \left[\frac{\partial(\mathbf{u}\cdot\mathbf{v})}{\partial t} - \mathbf{u}\cdot\frac{\partial \mathbf{v}}{\partial t}\right] \mathrm{d}t\mathrm{d}\Omega + \eta \int_0^T \int_\Omega \left[(\nabla\mathbf{u} + \nabla\mathbf{u}^{\mathrm{T}}) : \nabla\mathbf{v} - \nabla\cdot((\nabla\mathbf{u} + \nabla\mathbf{u}^{\mathrm{T}})\cdot\mathbf{v})\right] \mathrm{d}\Omega\mathrm{d}t \\ & + \int_0^T \int_\Omega \rho(\mathbf{u}\cdot\nabla)\mathbf{u}\cdot\mathbf{v}\ \mathrm{d}\Omega\mathrm{d}t + \int_0^T \int_\Omega [\nabla\cdot(p\mathbf{v}) - p\nabla\cdot\mathbf{v}]\ \mathrm{d}\Omega\mathrm{d}t - \int_0^T \int_\Omega \mathbf{f}\cdot\mathbf{v}\ \mathrm{d}\Omega\mathrm{d}t - \int_0^T \int_\Omega q\nabla\cdot\mathbf{u}\ \mathrm{d}\Omega\mathrm{d}t \\ & + \int_0^T \int_{\Gamma_N} \left[-p\mathbf{I} + \eta(\nabla\mathbf{u} + \nabla\mathbf{u}^{\mathrm{T}})\right]\mathbf{n}\cdot\mathbf{v}\ \mathrm{d}\Gamma\mathrm{d}t + \int_\Omega (\mathbf{u}\cdot\mathbf{v})\Big|_{t=0}\ \mathrm{d}\Omega \end{aligned} \tag{A.4}$$

Based on Gauss theory [45], Eq. (A.4) can be transformed into

$$\begin{aligned} e(\mathbf{u},p;\gamma) == {} & \rho \int_\Omega [(\mathbf{u}\cdot\mathbf{v})|_{t=T} - (\mathbf{u}\cdot\mathbf{v})|_{t=0}]\ \mathrm{d}\Omega - \rho \int_0^T \int_\Omega \mathbf{u}\cdot\frac{\partial\mathbf{v}}{\partial t}\ \mathrm{d}\Omega\mathrm{d}t + \eta \int_0^T \int_\Omega (\nabla\mathbf{u} + \nabla\mathbf{u}^{\mathrm{T}}) : \nabla\mathbf{v}\ \mathrm{d}\Omega\mathrm{d}t \\ & + \int_0^T \int_\Omega \rho(\mathbf{u}\cdot\nabla)\mathbf{u}\cdot\mathbf{v}\ \mathrm{d}\Omega\mathrm{d}t - \int_0^T \int_\Omega p\nabla\cdot\mathbf{v}\ \mathrm{d}\Omega\mathrm{d}t - \int_0^T \int_\Omega \mathbf{f}\cdot\mathbf{v}\ \mathrm{d}\Omega\mathrm{d}t \\ & + \int_0^T \int_{\partial\Omega} \left[p\mathbf{I} - \eta(\nabla\mathbf{u} + \nabla\mathbf{u}^{\mathrm{T}})\right]\mathbf{n}\cdot\mathbf{v}\ \mathrm{d}\Gamma\mathrm{d}t - \int_0^T \int_\Omega q\nabla\cdot\mathbf{u}\ \mathrm{d}\Omega\mathrm{d}t + \int_0^T \int_{\Gamma_D} \mathbf{u}\cdot\mathbf{v}\ \mathrm{d}\Gamma\mathrm{d}t \\ & + \int_0^T \int_{\Gamma_N} \left[-p\mathbf{I} + \eta(\nabla\mathbf{u} + \nabla\mathbf{u}^{\mathrm{T}})\right]\mathbf{n}\cdot\mathbf{v}\ \mathrm{d}\Gamma\mathrm{d}t + \int_\Omega (\mathbf{u}\cdot\mathbf{v})\Big|_{t=0}\ \mathrm{d}\Omega \end{aligned} \tag{A.5}$$

By inserting the boundary conditions into Eq. (A.5), the reduced weak operator of transient Navier–Stokes equations is obtained as

$$\begin{aligned} e(\mathbf{u},p;\gamma) = {} & \rho \int_\Omega [(\mathbf{u}\cdot\mathbf{v})|_{t=T} - \mathbf{u}_0\cdot\mathbf{v}|_{t=0}]\ \mathrm{d}\Omega - \rho \int_0^T \int_\Omega \mathbf{u}\cdot\frac{\partial\mathbf{v}}{\partial t}\ \mathrm{d}\Omega\mathrm{d}t + \eta \int_0^T \int_\Omega (\nabla\mathbf{u} + \nabla\mathbf{u}^{\mathrm{T}}) : \nabla\mathbf{v}\ \mathrm{d}\Omega\mathrm{d}t \\ & + \int_0^T \int_\Omega \rho(\mathbf{u}\cdot\nabla)\mathbf{u}\cdot\mathbf{v}\ \mathrm{d}\Omega\mathrm{d}t - \int_0^T \int_\Omega p\nabla\cdot\mathbf{v}\ \mathrm{d}\Omega\mathrm{d}t - \int_0^T \int_\Omega \mathbf{f}\cdot\mathbf{v}\ \mathrm{d}\Omega\mathrm{d}t - \int_0^T \int_\Omega q\nabla\cdot\mathbf{u}\ \mathrm{d}\Omega\mathrm{d}t \\ & + \int_0^T \int_{\Gamma_D} [p\mathbf{I} - \eta(\nabla\mathbf{u} + \nabla\mathbf{u}^{\mathrm{T}})\mathbf{n}\cdot\mathbf{v}]|_{\mathbf{u}=\mathbf{u}_D}\ \mathrm{d}\Gamma\mathrm{d}t + \int_0^T \int_{\Gamma_D} \mathbf{u}_D\cdot\mathbf{v}\ \mathrm{d}\Gamma\mathrm{d}t \end{aligned} \tag{A.6}$$

According to the definition of the Gâteaux derivative [45], the Gâteaux derivatives of Eq. (A.6) in the direction $(\mathbf{w},r) \in \mathbf{V}_\Omega \times \mathrm{V}_\Omega$ are

$$\begin{aligned} \langle e_{\mathbf{u}}(\mathbf{u},p;\gamma),\mathbf{w}\rangle_{\mathbf{V}_\Omega^*,\mathbf{V}_\Omega} = {} & \lim_{h\to 0^+} \frac{e(\mathbf{u}+h\mathbf{w},p) - e(\mathbf{u},p)}{h} = \rho \int_\Omega (\mathbf{w}\cdot\mathbf{v})|_{t=T}\ \mathrm{d}\Omega - \rho \int_0^T \int_\Omega \mathbf{w}\cdot\frac{\partial\mathbf{v}}{\partial t}\ \mathrm{d}t\mathrm{d}\Omega \\ & + \eta \int_0^T \int_\Omega (\nabla\mathbf{w} + \nabla\mathbf{w}^{\mathrm{T}}) : \nabla\mathbf{v}\ \mathrm{d}\Omega\mathrm{d}t + \int_0^T \int_\Omega \rho(\mathbf{w}\cdot\nabla)\mathbf{u}\cdot\mathbf{v}\ \mathrm{d}\Omega\mathrm{d}t + \int_0^T \int_\Omega \rho(\mathbf{u}\cdot\nabla)\mathbf{w}\cdot\mathbf{v}\ \mathrm{d}\Omega\mathrm{d}t \\ & - \int_0^T \int_\Omega \frac{\partial\mathbf{f}}{\partial\mathbf{u}}\mathbf{w}\cdot\mathbf{v}\ \mathrm{d}\Omega\mathrm{d}t - \int_0^T \int_\Omega q\nabla\cdot\mathbf{w}\ \mathrm{d}\Omega\mathrm{d}t \end{aligned} \tag{A.7}$$

and

$$\begin{aligned} \langle e_p(\mathbf{u},p;\gamma),r\rangle_{\mathrm{V}_\Omega^*,\mathrm{V}_\Omega} = {} & \lim_{h\to 0^+} \frac{e(\mathbf{u},p+hr) - e(\mathbf{u},p)}{h} \\ = {} & -\int_0^T \int_\Omega r\nabla\cdot\mathbf{v}\ \mathrm{d}\Omega\mathrm{d}t - \int_0^T \int_\Omega \frac{\partial\mathbf{f}}{\partial p} r\cdot\mathbf{v}\ \mathrm{d}\Omega\mathrm{d}t + \int_0^T \int_{\Gamma_D} r\mathbf{n}\cdot\mathbf{v}\ \mathrm{d}\Gamma\mathrm{d}t \end{aligned} \tag{A.8}$$

Based on the linear property of operators $\langle e_{\mathbf{u}}(\mathbf{u},p;\gamma),\mathbf{w}\rangle_{\mathbf{V}_\Omega^*,\mathbf{V}_\Omega}$ and $\langle e_p(\mathbf{u},p;\gamma),r\rangle_{\mathrm{V}_\Omega^*,\mathrm{V}_\Omega}$, they are bounded based on the Cauchy-Schwarz inequality and the Poincaré's inequality. Therefore, Eqs. (A.7) and (A.8) are the Gâteaux derivatives of $e(\mathbf{u},p)$. The dual operator of a linear operator is defined as [45]

$$\langle \mathcal{D}^* u, v\rangle_{\mathrm{X}^*,\mathrm{X}} = \langle u, \mathcal{D}v\rangle_{\mathrm{Y}^*,\mathrm{Y}}, \quad \forall u \in \mathrm{Y}^*, v \in \mathrm{X} \tag{A.9}$$

where X and Y are Banach spaces, $\mathcal{D} \in \mathcal{L}(\mathrm{X},\mathrm{Y})$ and $\mathcal{D}^* \in \mathcal{L}(\mathrm{Y}^*,\mathrm{X}^*)$. By rewriting $e_{\mathbf{u}}(\mathbf{u},p;\gamma)$ and $e_p(\mathbf{u},p;\gamma)$ in the formulation of linear operators, one can obtain

$$\begin{aligned} \langle e_{\mathbf{u}}(\mathbf{u},p;\gamma),\mathbf{w}\rangle_{\mathbf{V}_\Omega^*,\mathbf{V}_\Omega} &= \langle \mathcal{A}\mathbf{v} + \mathcal{B}q,\mathbf{w}\rangle_{\mathbf{V}_\Omega^*,\mathbf{V}_\Omega} \\ \langle e_p(\mathbf{u},p;\gamma),r\rangle_{\mathrm{V}_\Omega^*,\mathrm{V}_\Omega} &= \langle \mathcal{C}\mathbf{v},r\rangle_{\mathrm{V}_\Omega^*,\mathrm{V}_\Omega} \end{aligned} \tag{A.10}$$

and

$$\begin{aligned}\left\langle e^*_{\mathbf{u}}(\boldsymbol{\mu}, v; \gamma), \mathbf{w}\right\rangle_{\mathbf{V}^*_\Omega, \mathbf{V}_\Omega} &= \left\langle \mathcal{A}\boldsymbol{\mu} + \mathcal{B}v, \mathbf{w}\right\rangle_{\mathbf{V}^*_\Omega, \mathbf{V}_\Omega} \\ \left\langle e^*_p(\boldsymbol{\mu}, v; \gamma), r\right\rangle_{\mathrm{V}^*_\Omega, \mathrm{V}_\Omega} &= \langle \mathcal{C}\boldsymbol{\mu}, r\rangle_{\mathrm{V}^*_\Omega, \mathrm{V}_\Omega}\end{aligned} \tag{A.11}$$

where $\boldsymbol{\mu} \in \mathbf{V}_\Omega$ and $v \in \mathrm{V}_\Omega$, $\mathcal{A}, \mathcal{B}$ and $\mathcal{C}$ are linear operators. According to Eqs. (11) and (A.11), the weak form of the adjoint equations for the topology optimization problem of unsteady Navier–Stokes flows in Eq. (7) can be obtained as

$$\begin{aligned}&\rho \int_\Omega (\mathbf{w}\cdot\boldsymbol{\mu})\Big|_{t=T} \mathrm{d}\Omega - \rho \int_0^T \int_\Omega \mathbf{w}\cdot\frac{\partial \boldsymbol{\mu}}{\partial t}\,\mathrm{d}\Omega\mathrm{d}t + \eta \int_0^T \int_\Omega (\nabla\mathbf{w} + \nabla\mathbf{w}^{\mathrm{T}}) : \nabla\boldsymbol{\mu}\,\mathrm{d}\Omega\mathrm{d}t \\ &\quad + \int_0^T \int_\Omega \rho(\mathbf{w}\cdot\nabla)\mathbf{u}\cdot\boldsymbol{\mu}\,\mathrm{d}\Omega\mathrm{d}t + \int_0^T \int_\Omega \rho(\mathbf{u}\cdot\nabla)\mathbf{w}\cdot\boldsymbol{\mu}\,\mathrm{d}\Omega\mathrm{d}t - \int_0^T \int_\Omega v\nabla\cdot\mathbf{w}\,\mathrm{d}\Omega\mathrm{d}t - \int_0^T \int_\Omega \frac{\partial \mathbf{f}}{\partial \mathbf{u}}\mathbf{w}\cdot\boldsymbol{\mu}\,\mathrm{d}\Omega\mathrm{d}t \\ &= -\langle J_{\mathbf{u}}(\mathbf{u}, \nabla\mathbf{u}, p; \gamma), \mathbf{w}\rangle_{\mathbf{V}^*_\Omega, \mathbf{V}_\Omega}\end{aligned} \tag{A.12}$$

and

$$-\int_0^T \int_\Omega r\nabla\cdot\boldsymbol{\mu}\,\mathrm{d}\Omega\mathrm{d}t - \int_0^T \int_\Omega \frac{\partial \mathbf{f}}{\partial p} r\cdot\boldsymbol{\mu}\,\mathrm{d}\Omega\mathrm{d}t + \int_0^T \int_{\Gamma_D} r\mathbf{n}\cdot\boldsymbol{\mu}\,\mathrm{d}\Gamma\mathrm{d}t = -\langle J_p(\mathbf{u}, \nabla\mathbf{u}, p; \gamma), r\rangle_{\mathrm{V}^*_\Omega, \mathrm{V}_\Omega} \tag{A.13}$$

Additionally, there are

$$\int_0^T \int_\Omega (\nabla\mathbf{w} + \nabla\mathbf{w}^{\mathrm{T}}) : \nabla\boldsymbol{\mu}\,\mathrm{d}\Omega\mathrm{d}t = -\int_0^T \int_\Omega \nabla\cdot(\nabla\boldsymbol{\mu} + \nabla\boldsymbol{\mu}^{\mathrm{T}})\cdot\mathbf{w}\,\mathrm{d}\Omega\mathrm{d}t + \int_0^T \int_{\Gamma_N} (\nabla\boldsymbol{\mu} + \nabla\boldsymbol{\mu}^{\mathrm{T}})\mathbf{n}\cdot\mathbf{w}\,\mathrm{d}\Gamma\mathrm{d}t \tag{A.14}$$

$$\int_0^T \int_\Omega v\nabla\cdot\mathbf{w}\,\mathrm{d}\Omega\mathrm{d}t = -\int_0^T \int_\Omega \nabla v\cdot\mathbf{w}\,\mathrm{d}\Omega\mathrm{d}t + \int_0^T \int_{\Gamma_N} v\mathbf{n}\cdot\mathbf{w}\,\mathrm{d}\Gamma\mathrm{d}t \tag{A.15}$$

and

$$\int_0^T \int_\Omega (\mathbf{u}\cdot\nabla)\mathbf{w}\cdot\boldsymbol{\mu}\,\mathrm{d}\Omega\mathrm{d}t = -\int_0^T \int_\Omega (\mathbf{u}\cdot\nabla)\boldsymbol{\mu}\cdot\mathbf{w}\,\mathrm{d}\Omega\mathrm{d}t + \int_0^T \int_{\Gamma_N} (\mathbf{u}\cdot\mathbf{n})\boldsymbol{\mu}\cdot\mathbf{w}\,\mathrm{d}\Gamma\mathrm{d}t \tag{A.16}$$

Because $\mathbf{u}$ is known on Σ_D and p can be expressed by $\nabla\mathbf{u}$ on Σ_N, according to Eq. (4)

$$B(\mathbf{u}, p; \gamma) = \begin{cases} B(p; \gamma), & \text{on } \Sigma_D \\ B(\mathbf{u}, \nabla\mathbf{u}; \gamma), & \text{on } \Sigma_N \end{cases} \tag{A.17}$$

By inserting Eqs. (A.14)–(A.17) into Eqs. A.12 and A.13, one can obtain

$$\begin{aligned}\langle J_{\mathbf{u}}(\mathbf{u}, p; \gamma), \mathbf{w}\rangle_{\mathbf{V}^*_\Omega, \mathbf{V}_\Omega} &= \int_0^T \int_\Omega \beta_1 \left[\frac{\partial A}{\partial \mathbf{u}}\cdot\mathbf{w} - (\nabla\cdot\frac{\partial A}{\partial \nabla\mathbf{u}})\cdot\mathbf{w}\right]\mathrm{d}\Omega\mathrm{d}t + \int_0^T \int_{\Gamma_N} \beta_1 \frac{\partial A}{\partial \nabla\mathbf{u}}\mathbf{n}\cdot\mathbf{w}\,\mathrm{d}\Gamma\mathrm{d}t \\ &\quad + \int_0^T \int_{\Gamma_N} \beta_2 \frac{\partial B}{\partial \mathbf{u}}\cdot\mathbf{w}\,\mathrm{d}\Gamma\mathrm{d}t\end{aligned} \tag{A.18}$$

and

$$\langle J_p(\mathbf{u}, p; \gamma), r\rangle_{\mathrm{V}^*_\Omega, \mathrm{V}_\Omega} = \int_0^T \int_\Omega \beta_1 \frac{\partial A}{\partial p} r\,\mathrm{d}\Omega\mathrm{d}t + \int_0^T \int_{\Gamma_D} \beta_2 \frac{\partial B}{\partial p} r\,\mathrm{d}\Gamma\mathrm{d}t \tag{A.19}$$

Therefore, the adjoint equations of the Navier–Stokes equations can be written as

$$\begin{aligned}&-\rho\tfrac{\partial \boldsymbol{\mu}}{\partial t} - \eta\nabla\cdot(\nabla\boldsymbol{\mu} + \nabla\boldsymbol{\mu}^{\mathrm{T}}) - \rho(\mathbf{u}\cdot\nabla)\boldsymbol{\mu} + \rho(\nabla\mathbf{u})\cdot\boldsymbol{\mu} + \nabla v = -\beta_1\left(\tfrac{\partial A}{\partial \mathbf{u}} - \nabla\cdot\tfrac{\partial A}{\partial \nabla\mathbf{u}}\right) + \tfrac{\partial \mathbf{f}}{\partial \mathbf{u}}\boldsymbol{\mu}, \quad \text{in } Q \\ &-\nabla\cdot\boldsymbol{\mu} = -\beta_1\tfrac{\partial A}{\partial p} + \tfrac{\partial \mathbf{f}}{\partial p}\cdot\boldsymbol{\mu}, \quad \text{in } Q \\ &\boldsymbol{\mu}(T, \mathbf{x}) = \mathbf{0}, \quad \text{in } \Omega \\ &\boldsymbol{\mu} = -\tfrac{\partial B}{\partial p}\mathbf{n}, \quad \text{on } \Sigma_D \\ &[-v\mathbf{I} + \eta(\nabla\boldsymbol{\mu} + \nabla\boldsymbol{\mu}^{\mathrm{T}})]\mathbf{n} = -\rho(\mathbf{u}\cdot\mathbf{n})\boldsymbol{\mu} - \beta_1\tfrac{\partial A}{\partial \nabla\mathbf{u}}\mathbf{n} - \beta_2\tfrac{\partial B}{\partial \mathbf{u}}, \quad \text{on } \Sigma_N\end{aligned} \tag{A.20}$$

Appendix B. Adjoint sensitivity of optimization problem

Based on the similar analysis of the dual operator of $e_\gamma(\mathbf{u},p;\gamma)$, the adjoint derivatives of the optimization problem can be obtained as

$$\left\langle \frac{\widehat{DJ}}{D\gamma}, \psi \right\rangle_{L^\infty(\Omega), L^1(\Omega)} = \int_0^T \int_\Omega \left(\beta_1 \frac{\partial A}{\partial \gamma} + \frac{\partial \mathbf{f}}{\partial \gamma} \cdot \boldsymbol{\mu} \right) \psi \, d\Omega dt = \int_\Omega \int_0^T \left(\beta_1 \frac{\partial A}{\partial \gamma} + \frac{\partial \mathbf{f}}{\partial \gamma} \cdot \boldsymbol{\mu} \right) \psi \, dt d\Omega$$
$$= \int_\Omega \left[\int_0^T \left(\beta_1 \frac{\partial A}{\partial \gamma} + \frac{\partial \mathbf{f}}{\partial \gamma} \cdot \boldsymbol{\mu} \right) dt \right] \psi \, d\Omega \tag{B.1}$$

and

$$\left\langle \frac{\widehat{DJ}}{D\gamma}, \psi \right\rangle_{L^\infty(\partial\Omega), L^1(\partial\Omega)} = \int_0^T \int_{\partial\Omega} \beta_2 \frac{\partial B}{\partial \gamma} \psi \, d\Gamma dt = \int_{\partial\Omega} \left[\int_0^T \beta_2 \frac{\partial B}{\partial \gamma} \, dt \right] \psi \, d\Gamma \tag{B.2}$$

where $\forall \psi \in C^\infty(\bar{\Omega})$. Therefore, according to Eq. (12), the adjoint derivatives can be expressed as

$$\begin{aligned} &\left. \frac{\widehat{DJ}}{D\gamma} \right|_\Omega = \int_0^T \left(\beta_1 \tfrac{\partial A}{\partial \gamma} - \tfrac{\partial \alpha}{\partial \gamma} \mathbf{u} \cdot \boldsymbol{\mu} \right) dt, \quad \text{in } \Omega \\ &\left. \frac{\widehat{DJ}}{D\gamma} \right|_{\partial\Omega} = \int_0^T \beta_2 \tfrac{\partial B}{\partial \gamma} \, dt, \quad \text{on } \partial\Omega \end{aligned} \tag{B.3}$$

Appendix C. Adjoint analysis of expression defined on $[T_1, T_2] \subseteq [0, T]$

In some cases, the expression in Eq. (8) is defined on the subset $[T_1, T_2]$ instead of $[0, T]$:

$$J(\mathbf{u}, p; \gamma) = \int_{T_1}^{T_2} \int_\Omega \beta_1 A(\mathbf{u}, \nabla \mathbf{u}, p; \gamma) \, d\Omega dt + \int_{T_1}^{T_2} \int_{\partial\Omega} \beta_2 B(\mathbf{u}, p; \gamma) \, d\Gamma dt \tag{C.1}$$

where $[T_1, T_2]$ is a subset of $[0, T]$. Then Eq. (C.1) can be rewritten as

$$\begin{aligned} J(\mathbf{u}, p; \gamma) = &\int_0^{T_1} \int_\Omega 0 \, d\Omega dt + \int_0^{T_1} \int_{\partial\Omega} 0 \, d\Gamma dt + \int_{T_1}^{T_2} \int_\Omega \beta_1 A(\mathbf{u}, \nabla \mathbf{u}, p; \gamma) \, d\Omega dt + \int_{T_1}^{T_2} \int_{\partial\Omega} \beta_2 B(\mathbf{u}, p; \gamma) \, d\Gamma dt \\ &+ \int_{T_2}^{T} \int_\Omega 0 \, d\Omega dt + \int_{T_2}^{T} \int_{\partial\Omega} 0 \, d\Gamma dt \end{aligned} \tag{C.2}$$

where A and B are set to 0 in $(0, T_1)$ and (T_1, T_2), respectively. Then Eqs. (A.18) and (A.19) can be rewritten as

$$\begin{aligned} \langle J_{\mathbf{u}}(\mathbf{u}, p; \gamma), \mathbf{w} \rangle_{\mathbf{V}_\Omega^*, \mathbf{V}_\Omega} = &\int_0^{T_1} \int_\Omega 0 \, d\Omega dt + \int_0^{T_1} \int_{\Gamma_N} 0 \, d\Gamma dt + \int_0^{T_1} \int_{\Gamma_N} 0 \, d\Gamma dt + \int_{T_1}^{T_2} \\ &\times \int_\Omega \beta_1 \left[\frac{\partial A}{\partial \mathbf{u}} \cdot \mathbf{w} - \left(\nabla \cdot \frac{\partial A}{\partial \nabla \mathbf{u}} \right) \cdot \mathbf{w} \right] d\Omega dt + \int_{T_1}^{T_2} \int_{\Gamma_N} \beta_1 \frac{\partial A}{\partial \nabla \mathbf{u}} \mathbf{n} \cdot \mathbf{w} \, d\Gamma dt + \int_{T_1}^{T_2} \int_{\Gamma_N} \beta_2 \frac{\partial B}{\partial \mathbf{u}} \\ &\cdot \mathbf{w} d\Gamma dt + \int_{T_2}^{T} \int_\Omega 0 \, d\Omega dt + \int_{T_2}^{T} \int_{\Gamma_N} 0 \, d\Gamma dt + \int_{T_2}^{T} \int_{\Gamma_N} 0 \, d\Gamma dt \end{aligned} \tag{C.3}$$

and

$$\begin{aligned} \langle J_p(\mathbf{u}, p; \gamma), r \rangle_{V_\Omega^*, V_\Omega} = &\int_0^{T_1} \int_\Omega 0 \, d\Omega dt + \int_{T_1}^{T_2} \int_\Omega \beta_1 \frac{\partial A}{\partial p} r \, d\Omega dt + \int_{T_2}^{T} \int_\Omega 0 \, d\Omega dt + \int_0^{T_1} \int_{\Gamma_D} 0 \, d\Gamma dt \\ &+ \int_{T_1}^{T_2} \int_{\Gamma_D} \beta_2 \frac{\partial B}{\partial p} r \, d\Gamma dt + \int_{T_2}^{T} \int_{\Gamma_D} 0 \, d\Gamma dt \end{aligned} \tag{C.4}$$

Therefore, the adjoint equations of the Navier–Stokes equations can be written as

When $t \in (T_2, T)$

$$\begin{aligned} &-\rho \tfrac{\partial \boldsymbol{\mu}}{\partial t} - \eta \nabla \cdot (\nabla \boldsymbol{\mu} + \nabla \boldsymbol{\mu}^{\mathrm{T}}) - \rho (\mathbf{u} \cdot \nabla) \boldsymbol{\mu} + \rho (\nabla \mathbf{u}) \cdot \boldsymbol{\mu} + \nabla v = \tfrac{\partial \mathbf{f}}{\partial \mathbf{u}} \boldsymbol{\mu}, \quad \text{in} (T_2, T) \times \Omega \\ &-\nabla \cdot \boldsymbol{\mu} = \tfrac{\partial \mathbf{f}}{\partial p} \cdot \boldsymbol{\mu}, \quad \text{in} (T_2, T) \times \Omega \\ &\boldsymbol{\mu}(T, \mathbf{x}) = \mathbf{0}, \quad \text{in } \Omega \\ &\boldsymbol{\mu} = \mathbf{0}, \text{on } (T_2, T) \times \Gamma_D \\ &[-v\mathbf{I} + \eta (\nabla \boldsymbol{\mu} + \nabla \boldsymbol{\mu}^{\mathrm{T}})] \mathbf{n} = -\rho (\mathbf{u} \cdot \mathbf{n}) \boldsymbol{\mu}, \quad \text{on } (T_2, T) \times \Gamma_N \end{aligned} \tag{C.5}$$

When $t \in (T_1, T_2)$

$$\begin{aligned}
&-\rho\tfrac{\partial \boldsymbol{\mu}}{\partial t} - \eta\nabla\cdot(\nabla\boldsymbol{\mu} + \nabla\boldsymbol{\mu}^{\mathrm{T}}) - \rho(\mathbf{u}\cdot\nabla)\boldsymbol{\mu} + \rho(\nabla\mathbf{u})\cdot\boldsymbol{\mu} + \nabla v = -\beta_1\left(\tfrac{\partial A}{\partial \mathbf{u}} - \nabla\cdot\tfrac{\partial A}{\partial \nabla\mathbf{u}}\right) + \tfrac{\partial \mathbf{f}}{\partial \mathbf{u}}\boldsymbol{\mu}, \quad \text{in } (T_1,T_2)\times\Omega \\
&-\nabla\cdot\boldsymbol{\mu} = -\beta_1\tfrac{\partial A}{\partial p} + \tfrac{\partial \mathbf{f}}{\partial p}\cdot\boldsymbol{\mu}, \quad \text{in } (T_1,T_2)\times\Omega \\
&\boldsymbol{\mu} = -\tfrac{\partial B}{\partial p}\mathbf{n}, \quad \text{on } (T_1,T_2)\times\Gamma_D \\
&\left[-v\mathbf{I} + \eta(\nabla\boldsymbol{\mu} + \nabla\boldsymbol{\mu}^{\mathrm{T}})\right]\mathbf{n} = -\rho(\mathbf{u}\cdot\mathbf{n})\boldsymbol{\mu} - \beta_1\tfrac{\partial A}{\partial \nabla\mathbf{u}}\mathbf{n} - \beta_2\tfrac{\partial B}{\partial \mathbf{u}}, \quad \text{on } (T_1,T_2)\times\Gamma_N
\end{aligned} \tag{C.6}$$

When $t \in (0, T_1)$

$$\begin{aligned}
&-\rho\tfrac{\partial \boldsymbol{\mu}}{\partial t} - \eta\nabla\cdot(\nabla\boldsymbol{\mu} + \nabla\boldsymbol{\mu}^{\mathrm{T}}) - \rho(\mathbf{u}\cdot\nabla)\boldsymbol{\mu} + \rho(\nabla\mathbf{u})\cdot\boldsymbol{\mu} + \nabla v = \tfrac{\partial \mathbf{f}}{\partial \mathbf{u}}\boldsymbol{\mu}, \quad \text{in } (0,T_1)\times\Omega \\
&-\nabla\cdot\boldsymbol{\mu} = \tfrac{\partial \mathbf{f}}{\partial p}\cdot\boldsymbol{\mu}, \text{in}(0,T_1)\times\Omega \\
&\boldsymbol{\mu} = \mathbf{0}, \quad \text{on } (0,T_1)\times\Gamma_D \\
&[-v\mathbf{I} + \eta(\nabla\boldsymbol{\mu} + \nabla\boldsymbol{\mu}^{\mathrm{T}})]\mathbf{n} = -\rho(\mathbf{u}\cdot\mathbf{n})\boldsymbol{\mu}, \quad \text{on } (0,T_1)\times\Gamma_N
\end{aligned} \tag{C.7}$$

By solving Eqs. (C.5), (C.6) and (C.7) sequentially, the adjoint variables of $\mathbf{u}$ and p can be obtained. Because the solution of Eq. (C.5) is $\boldsymbol{\mu} = \mathbf{0}$ and $v = 0$, one only needs to solved Eqs. (C.6) and (C.7) with the initial condition $\boldsymbol{\mu}(T_2,\mathbf{x}) = \mathbf{0}$. The adjoint derivatives corresponding to expression (C.1) can be expressed as

$$\begin{aligned}
&\widehat{\tfrac{DJ}{D\gamma}}|_{\Omega} = \int_{T_1}^{T_2}\left(\beta_1\tfrac{\partial A}{\partial \gamma} - \tfrac{\partial \alpha}{\partial \gamma}\mathbf{u}\cdot\boldsymbol{\mu}\right)\mathrm{d}t + \int_0^{T_1} -\tfrac{\partial \alpha}{\partial \gamma}\mathbf{u}\cdot\boldsymbol{\mu}\,\mathrm{d}t, \quad \text{in } \Omega \\
&\widehat{\tfrac{DJ}{D\gamma}}|_{\partial\Omega} = \int_{T_1}^{T_2}\beta_2\tfrac{\partial B}{\partial \gamma}\,\mathrm{d}t, \quad \text{on } \partial\Omega
\end{aligned} \tag{C.8}$$

Therefore, the adjoint analysis of the objective or design constraints defined on the subinterval $[T_1, T_2] \subseteq [0, T]$ is implemented on $[0, T_2]$ instead of $[0, T]$, although the unsteady flow problem is defined on the time interval $[0, T]$. Subsequently, the corresponding adjoint equations and adjoint derivatives are transient equations and integrations on $[0, T_2]$ instead of $[0, T]$, respectively.

References

[1] G.I.N. Rozvany, Aims, scope, methods, history and unified terminology of computer-aided topology optimization in structural mechanics, Struct. Multidisc. Optim. 21 (2001) 90–108.
[2] M.P. Bendsϕe, O. Sigmund, Material interpolations in topology optimization, Arch. Appl. Mech. 69 (1999) 635–654.
[3] M.Y. Wang, X. Wang, D. Guo, A level set method for structural optimization, Comput. Methods Appl. Mech. Eng. 192 (2003) 227–246.
[4] G. Allaire, F. Jouve, A. Toader, Structural optimization using sensitivity analysis and a level-set method, J. Comput. Phys. 194 (2004) 363–393.
[5] Z. Liu, J.G. Korvink, Adaptive moving mesh level set method for structure optimization, Eng. Optim. 40 (2008) 529–558.
[6] X. Xing, P. Wei, M.Y. Wang, A finite element-based level set method for structural optimization, Int. J. Numer. Methods Eng. 82 (2010) 805–842.
[7] M.P. Bendsϕe, N. Kikuchi, Generating optimal topologies in optimal design using a homogenization method, Comput. Methods Appl. Mech. Eng. 71 (1988) 197–224.
[8] O. Sigmund, A 99-line topology optimization code written in Matlab, Struct. Multidisc. Optim. 21 (2001) 120–127.
[9] O. Sigmund, On the design of compliant mechanisms using topology optimization, Mech. Struct. Mach. 25 (1997) 495–526.
[10] A. Saxena, Topology design of large displacement compliant mechanisms with multiple materials and multiple output ports, Struct. Multidisc. Optim. 30 (2005) 477–490.
[11] M. Bendsϕe, O. Sigmund, Topology Optimization-Theory Methods and Applications, Springer, 2003.
[12] T. Borrvall, J. Petersson, Topology optimization of fluid in Stokes flow, Int. J. Numer. Methods Fluids 41 (2003) 77–107.
[13] A. Gersborg-Hansen, M.P. Bendsϕe, O. Sigmund, Topology optimization of heat conduction problems using the finite volume method, Struct. Multidisc. Optim. 31 (2006) 251–259.
[14] T. Nomura, K. Sato, K. Taguchi, T. Kashiwa, S. Nishiwaki, Structural topology optimization for the design of broadband dielectric resonator antennas using the finite difference time domain technique, Int. J. Numer. Methods Eng. 71 (2007) 1261–1296.
[15] O. Sigmund, K.G. Hougaard, Geometric properties of optimal photonic crystals, Phys. Rev. Lett. 100 (2008) 153904.
[16] M.B. Duhring, J.S. Jensen, O. Sigmund, Acoustic design by topology optimization, J. Sound Vibr. 317 (2008) 557–575.
[17] W. Akl, A. El-Sabbagh, K. Al-Mitani, A. Baz, Topology optimization of a plate coupled with acoustic cavity, Int. J. Solids Struct. 46 (2008) 2060–2074.
[18] P.H. Guillaume, K.S. Idris, Topological sensitivity and shape optimization for the Stokes equations, SIAM J. Cont. Optim. 43 (2004) 1–31.
[19] N. Aage, T.H. Poulsen, A. Gersborg-Hansen, O. Sigmund, Topology optimization of large scale stokes flow problems, Struct. Multidisc. Optim. 35 (2008) 175–180.
[20] J.K. Guest, J.H. Proevost, Topology optimization of creeping fluid flows using a Darcy–Stokes finite element, Int. J. Numer. Methods Eng. 66 (2006) 461–484.
[21] N. Wiker, A. Klarbring, T. Borrvall, Topology optimization of regions of Darcy and Stokes flow, Int. J. Numer. Methods Eng. 69 (2007) 1374–1404.
[22] A. Gersborg-Hansen, O. Sigmund, R.B. Haber, Topology optimization of channel flow problems, Struct. Multidisc. Optim. 29 (2005) 1–12.
[23] L.H. Olesen, F. Okkels, H. Bruus, A high-level programming-language implementation of topology optimization applied to steady-state Navier–Stokes flow, Int. J. Numer. Methods Eng. 65 (2006) 975–1001.
[24] A. Evgrafov, Topology optimization of slightly compressible fluids, ZAMM 86 (2006) 46–62.
[25] X. Duan, Y. Ma, R. Zhang, Shape-topology optimization for Navier–Stokes problem using variational level set method, J. Comput. Appl. Math. 222 (2008) 487–499.
[26] S. Zhou, Q. Li, A variational level set method for the topology optimization of steady-state Navier–Stokes flow, J. Comput. Phys. 227 (2008) 10178–10195.
[27] G. Pingen, K. Maute, Optimal design for non-Newtonian flows using a topology optimization approach, Comput. Math. Appl. 59 (2010) 2340–2350.
[28] F. Okkels, L.H. Olesen, H. Bruus, Application of topology optimization in the design of micro and nanofluidic systems, NSTI-Nanotech (2005) 575–578.
[29] F. Okkels, H. Bruus, Scaling behavior of optimally structured catalytic microfluidic reactors, Phys. Rev. E 75 (2007) 1–4.
[30] C.S. Andreasen, A.R. Gersborg, O. Sigmund, Topology optimization of microfluidic mixers, Int. J. Numer. Methods Fluids 61 (2008) 498–513.
[31] Y.B. Deng, Z.Y. Liu, P. Zhang, Y.H. Wu, J.G. Korvink, Optimization of no-moving-part fluidic resistance microvalves with low Reynolds number, in: IEEE MEMS Conference, 2010, pp. 67–70.

[32] S. Osher, J.A. Sethian, Front propagating with curvature dependent speed: algorithms based on Hamilton–Jacobi formulations, J. Comput. Phys. 78 (1988) 12–49.
[33] J. Sokolowski, A. Zochowski, On the topological derivative in shape optimization, SIAM J. Control Optim. 37 (1999) 1241–1272.
[34] J. Sokolowski, A. Zochowski, Topological derivatives for elliptic problems, Inverse Problems 15 (1999) 123–134.
[35] A.A. Novotny, R.A. Feijoo, E. Taroco, C. Padra, Topological sensitivity analysis, Comput. Methods Appl. Mech. Eng. 192 (2003) 803–829.
[36] M. Burger, B. Hackl, W. Ring, Incorporating topological derivatives into level set methods, J. Comput. Phys 194 (2004) 344–362.
[37] S. Amstutz, Topological sensitivity analysis for some nonlinear PDE systems, J. Math. Pures Appl. 85 (2006) 540–557.
[38] V.J. Challis, J.K. Guest, Level set topology optimization of fluids in Stokes flow, Int. J. Numer. Methods Eng. 79 (2009) 1284–1308.
[39] M. Abdelwahed, M. Hassine, Topological optimization method for a geometric control problem in Stokes flow, Appl. Numer. Math. 59 (2009) 1823–1838.
[40] H. Maatoug, Shape optimization for the Stokes equations using topological sensitivity analysis, ARIMA 5 (2006) 216–229.
[41] M.Y. Wang, Shape optimization with level set method incorporating topological derivatives, in: Sixth Congresses of Struc. Multidisc. Optim., 2005.
[42] S. Amstutz, The topological asymptotic for the Navier–Stokes equations, ESAIM: Control Optimization and Calculus of Variations 11 (2005) 401–425.
[43] D.N. Srinath, S. Mittal, An adjoint method for shape optimization in unsteady viscous flows, J. Comput. Phys. 229 (2010) 1994–2008.
[44] C. Brandenburg, F. Lindemann, M. Ulbrich, S. Ulbrich, A continuous adjoint approach to shape optimization for Navier–Stokes flow, Int. Ser. Numer. Math. 158 (2009) 35–56.
[45] M. Hinze, R. Pinnau, M. Ulbrich, S. Ulbrich, Optimization with PDE constraints, Springer, 2009.
[46] S. Kreissl, G. Pingen, K. Maute, Topology optimization for unsteady flow, Int. J. Numer. Meth. Eng. (2011), doi:10.1002/nme.3151.
[47] R.L. Panton, Incompressible flow, Wiley, 1984.
[48] M.B. Giles, N.A. Pierce, An introduction to the adjoint approach to design, Flow Turbulence Combust. 65 (2000) 393–415.
[49] B. Mohammadi, O. Pironneau, Applied shape optimization for fluids, OXFORD, 2010
[50] J. Nocedal, S.J. Wright, Numerical Optimization, Springer, 1998.
[51] E. Zeidler, Nonlinear Functional Analysis its Applications. I, Fixed-Point Theorems, Springer, 1986.
[52] <http://www.comsol.com>.
[53] K. Svanberg, The method of moving asymptotes: a new method for structural optimization, Int. J. Numer. Methods Eng. 24 (1987) 359–373.
[54] H.C. Elman, D.J. Silvester, A.J. Wathen, Finite elements and fast iterative solvers: with applications in incompressible fluid dynamics, OXFORD, 2006
[55] U.M. Ascher, L.R. Petzold, Computer Methods for Ordinary Differential Equations and Differential-Algebraic Equations, SIAM, 1998.
[56] D.J. Laser, J.G. Santiago, A review of micropumps, J. Micromech. Microeng. 14 (2004) 35–64.
[57] P. Chen, X. Feng, J. Sun, Y. Wang, W. Du, B.F. Liu, Hydrodynamic gating for sample introduction on a microfluidic chip, Lab on a chip 10 (2010) 1472–1475.
[58] A. Gersborg-Hansen, M. Berggren, B. Dammann, Topology optimization of mass distribution problems in Stokes flow, Solid Mech. Appl. 137 (2006) 365–374.
[59] C.H. Li Paul, Microfluidic Lab-on-a-Chip for Chemical and Biological Analysis and Discovery, CRC Press, 2005.
[60] J. Ducrée, S. Haeberle, S. Lutz, S. Pausch, F. Stetten, R. Zengerle, Design and fabrication of a centrifugally driven microfluidic disk for fully integrated metabolic assays on whole blood, J. Micromech. Microeng. 17 (2007) 103–115.
[61] K. Yosida, Functional Analysis, Springer, Berlin, 1980.